J Mater Sci: Mater Electron (2026) 37:1283

Comparative investigation on structural, superconducting, and magnetic properties of Zn-doped YBCO-123 and YBCO-358 phases synthesized by sol–gel method

G. Guducu[1], O. Ozturk[1], S. Kurnaz[2], T. Seydioglu[3], E. Asikuzun Tokeser[4], G. Yildirim[5,*], and S. Safran[6,7]

[1] *Department of Electrical and Electronics Engineering, Kastamonu University, 37210 Kastamonu, Turkey*
[2] *Central Research Laboratory, Kastamonu University, 37210 Kastamonu, Turkey*
[3] *Department of Electronics and Automation, Kastamonu Vocational School, Kastamonu University, 37210 Kastamonu, Turkey*
[4] *Department of Metallurgy and Materials Engineering, Kastamonu University, 37210 Kastamonu, Turkey*
[5] *Department of Mechanical Engineering, Bolu Abant Izzet Baysal University, 14280 Bolu, Turkey*
[6] *Department of Physics, Ankara University, 06100 Ankara, Turkey*
[7] *Ctr Excellence Superconduct Res, 50 Year Campus, 06830 Ankara, Turkey*

Received: 26 February 2026
Accepted: 1 June 2026

© The Author(s), 2026

ABSTRACT

This study investigates the structural, electrical, and magnetic properties of $YBa_2Cu_{3-x}Zn_xO_{7-\delta}$ (Y-123) and $Y_3Ba_5Cu_{8-x}Zn_xO_{18-\delta}$ (Y-358) superconductors synthesized via the sol–gel method, where copper sites were partially substituted with zinc ($x = 0.00$–0.15). Dense polycrystalline samples were obtained following calcination, sintering, and final heat treatment at 930 °C. Structural and microstructural changes with Zn doping were characterized using X-ray diffraction (XRD), scanning electron microscopy (SEM), and energy-dispersive spectroscopy (EDS), while electrical-superconducting and magnetic properties were determined by resistivity (ρ–T) and vibrating sample magnetometry (VSM) measurements. X-ray diffraction and SEM analyses show that Zn doping up to $x = 0.05$ preserves phase purity and structural stability in both Y-123 and Y-358, whereas higher Zn contents ($x \geq 0.10$) induce crystallographic disorder, secondary phases, reduced grain size, and increased porosity, particularly in the Y-358 superconducting phase. Electrical measurements reveal a systematic suppression of critical transition temperature, broadening of the transition, and reduced mobile hole concentration with Zn/Cu substitution, driving both systems into the underdoped regime due to reduced hole concentration, enhanced carrier scattering, and disorder in the Cu-O_2 planes. In other words, excess Zn disrupts the stabilization of superconducting clusters, weakens electronic bridging, and alters the density of states near the Fermi level, degrading superconductivity through both structural

Address correspondence to E-mail: yildirim_g@ibu.edu.tr

https://doi.org/10.1007/s10854-026-17713-y
Published online: 09 June 2026

and electronic localization effects. Magnetic characterizations confirm a strong reduction in critical current density (J_c) and flux pinning force (F_p) with Zn doping, linked to pair-breaking and vortex mobility arising from nonmagnetic Zn^{2+} ions in the active CuO_2 planes. Compared with Y-358, the Y-123 phase exhibits greater tolerance to Zn-induced disorder and more stable pinning characteristics. These findings provide comparative information about the role of Zn doping in modulating charge carrier dynamics, flux pinning, and superconducting stability of Y-123 and Y-358 phases, underscoring the importance of compositional control for high-T_c superconductor optimization.

1 Introduction

The fabrication of high-performance high-temperature superconductors (HTS) demands careful optimization of multiple parameters, including the synthesis route, dopant type and concentration, and sintering conditions (temperature, duration, and oxygen partial pressure) due to the determination of the final structural, electronic, and superconducting properties of the materials. Among the available synthesis techniques, the sol–gel (SG) method provides distinct advantages, such as compositional homogeneity, high-purity, stoichiometrically controlled production, nanoscale mixing, and effective dopant incorporation, enabling the preparation of high-quality bulk YBCO superconductors. Sol–gel-derived powders, when pressed into pellets and subjected to optimized sintering treatments, typically exhibit improved grain connectivity, enhanced superconducting phase purity, and superior critical transition temperature and critical current density values, establishing the method as an indispensable tool in advancing HTS technologies [1].

The superconducting properties of YBCO are intimately tied to its layered perovskite-type crystal structure, particularly the adjacent active CuO_2 in-plane layers that serve as the primary conduction pathways for Cooper pairs. Substitutions at the Cu, Y, or Ba sites or intercalations in Cu–O chains and planes can substantially alter superconducting parameters, as they directly affect the electronic environment of Cu–O bonds and modify the hybridization between Cu-3d and O-2p orbitals [2, 3]. Homo- and aliovalent substitutions at Cu sites are especially influential, as they alter charge carrier densities and local spin correlations, hence modulating electrical-superconducting and flux pinning ability [4–6]. Considerable efforts have therefore been directed toward introducing nanoparticles or dopants into YBCO systems to enhance flux pinning, magnetic performance, interlayer Josephson coupling, vortex lattice elasticity, and suppress weak-link coupling effects at grain boundaries and energy dissipation mechanisms arising from the thermally activated motion of discrete 2D pancake vortices. However, outcomes are often contradictory, depending on ionic radius, valence state, and chemical compatibility with the host lattice of the dopant atoms [7–13].

Zinc substitution, in particular, has been shown to strongly suppress critical transition temperatures in YBCO superconducting phases, attributed to the disruption of weakly coupled copper oxide planes, localization of charge carriers, and increased oxygen deficiency [10, 14–25]. In this context, spinless Zn^{2+} ions not only disturb long-range antiferromagnetic order but also act as pair-breaking centers within the active CuO_2 consecutively stacked planes, leading to structural disorder, altered Cu–O bond lengths, and weakened interlayer charge transfer mechanism along the crystal system. Post-synthesis thermal treatments have further demonstrated that Zn migration can intensify oxygen loss, and accelerate the deterioration of superconductivity.

While the conventional Y-123 superconducting phase remains the most widely studied member of the YBCO parents, extended phases such as Y-358 have attracted increasing interest. First reported by Aliabadi et al. [26], Y-358 superconducting phase exhibits a higher critical transition temperature (T_c), higher than 100 K, and a more complex crystal

structure comprising five active Cu-O_2 planes and three Cu–O chains per unit cell, compared to only two planes and one chain in the Y-123 superconducting ceramic phase. The structural complexity of Y-358 is reflected in its elongated *c*-axis parameter and higher oxygen content [27, 28], both of which are strongly sensitive to synthesis conditions. Regardless, achieving phase-pure Y-358 remains challenging due to its structural instability and intergrowth with Y-123 and Y-124 phases [29–36]. Besides, reports in the literature reveal inconsistent findings on its T_c and lattice parameters, highlighting the need for further systematic investigations [37–44].

Despite significant advances, several fundamental limitations persist in YBCO-based superconductors. The presence of weak links at grain boundaries and thermally activated vortex motion severely limit critical current density (J_c depending on the flux pinning centers, and vortex lattice elasticity), especially under applied magnetic fields. On this basis, enhancing flux pinning through the introduction of artificial pinning centers at the nanoscale has been widely explored, but inconsistencies remain due to the complex interplay of structural strain, lattice distortions, and dopant–host interactions [45–51]. Accordingly, comparative investigations of different YBCO phases under controlled doping are critical for clarifying the relationship between structural modifications, electrical transport, superconducting, and magnetic performance. The present work focuses on Y-123 and Y-358 phases, where Zn substitution at Cu sites is systematically examined to evaluate its influence on microstructural evolution, charge carrier concentration, fluctuation-induced conductivity, and fundamental magnetic performances, including pinning energy and carrying critical current density capacity. Samples were synthesized via the sol–gel route to ensure compositional homogeneity, and characterized by X-ray diffraction (XRD), scanning electron microscopy (SEM), energy-dispersive spectroscopy (EDS), resistivity (ρ–T) analysis, and vibrating sample magnetometry (VSM). By correlating structural, electrical, and magnetic properties, this study aims to clarify the mechanisms underlying Zn-induced modifications in Y-123 and Y-358 ceramic systems, thus contributing both to the fundamental understanding of HTS materials and their potential technological applications.

2 Materials and methods

2.1 Sample preparation

In this study, zinc ions were partially substituted with copper (Cu) ions in four different molar ratios ($x = 0.01$, 0.05, 0.10, and 0.15) to synthesize two superconducting phases of the YBCO family: $YBa_2Cu_{3-x}(Zn)_xO_{1-\delta}$ (Y-123) and $Y_3Ba_5Cu_{8-x}(Zn)_xO_{18-\delta}$ (Y-358) superconducting phases. All samples were prepared using the sol–gel technique to ensure homogeneity of chemical composition. Yttrium(III) acetate hydrate [$Y(CH_3COO)_3{\cdot}xH_2O$], barium acetate [$Ba(CH_3COO)_2$], copper(II) acetate [$Cu(CH_3COO)_2$], zinc (Zn), and terbium (Tb) nano powders were used as the starting precursors. Anhydrous methanol (CH_3OH) was employed as a diluent, glacial acetic acid (CH_3COOH) as a solvent, and triethanolamine (tri(2-hydroxyethyl) amine) as both a thickener and pH regulator to form a wet sol–gel solution. The mixture was stirred at room temperature for 12 h in a parafilm-sealed beaker until a bluish transparent solution was obtained. The solution was then gradually heated from 800 °C to 1000 °C in an open beaker, resulting in a brown foamy gel, which was subsequently placed in an ash oven at 350 °C for 1 h to promote hydration. After cooling, the dried gel was collected, ground into powder using an agate mortar, and calcined in an alumina crucible at 850 °C. This calcination and grinding process was repeated at least three times over a 24-h period to achieve uniform nano-crystallinity. The resulting nano powders were pressed into 10 mm pellets and sintered at 930 °C for 24 h at a heating rate of 5 °C/min. Following sintering, the samples were cooled to 500 °C within 1 h and exposed to flowing oxygen at this temperature for 5 h to optimize oxygen content, before finally being cooled to room temperature. This process yielded dense ceramic samples suitable for further characterization. The Zn-doped Y-123 samples were labeled as Y1, Y1Z1, Y1Z5, Y1Z10, and Y1Z15, while the corresponding Y-358 samples were denoted as Y3, Y3Z1, Y3Z5, Y3Z10, and Y3Z15, respectively, according to their Zn content ($x = 0.01$, 0.05, 0.10, and 0.15).

2.2 Characterization

XRD patterns of the synthesized bulk ceramic samples were recorded using a Bruker D8 Advance model X-ray

diffractometer equipped with a CuKα radiation source ($\lambda = 1.541$ Å). The measurements were conducted in the 2θ range of 10° to 70° with a scanning rate of 3°/min under ambient conditions. The diffractometer was operated in continuous scan mode to ensure high-resolution data acquisition suitable for detailed structural analysis. The crystallographic information was derived from the resulting diffraction peaks, and the interplanar spacing (d) values were calculated using Bragg's law given in Eq. (1):

$$n\lambda = 2d \sin\theta \tag{1}$$

where λ is the wavelength of the incident X-rays, θ is the Bragg's angle, d is the interplanar spacing, and n is the order of reflection (taken as 1 for simplicity). The corresponding Miller indices (hkl) were assigned to the prominent diffraction peaks based on standard reference diffracted patterns, and lattice cell parameters were further evaluated using the following equation for orthorhombic or tetragonal crystal systems using Eq. (2):

$$\frac{1}{d^2} = \frac{h^2}{a^2} + \frac{k^2}{b^2} + \frac{l^2}{c^2} \tag{2}$$

This structural analysis enabled phase identification, evaluation of crystalline quality, and estimation of lattice distortions, providing critical information about the effects of Zn doping on the Y-123 and Y-358 superconducting phases.

The lattice parameters a, b, and c correspond to the unit cell dimensions of the orthorhombic crystal structure and were determined from the indexed XRD diffraction patterns. The average crystallite size (D) belonging to the ceramic samples was estimated using the well-known Warren–Scherrer equation (Eq. (3)), which relates peak broadening in the XRD pattern to the size of coherently diffracting domains:

$$D = \frac{0.941\lambda}{B\cos\theta} \tag{3}$$

In this expression, D is the crystallite size (in nanometers), λ is the X-ray wavelength (1.541 Å for CuK_α radiation), B is the corrected full width at half maximum (FWHM) of the diffraction peak (in radians), and θ is the corresponding Bragg angle. The peak broadening B was corrected for instrumental effects using Eq. (4):

$$B^2 = B_s^2 - B_m^2 \tag{4}$$

where B_s is the experimentally measured FWHM of the diffraction peak, and B_m is the instrumental broadening constant, taken as 0.000007 rad for the applied system. This correction ensures a more accurate estimation of the crystallite size by eliminating contributions from instrumental limitations.

In addition, the orthorhombicity coefficient (δ) was calculated to quantify the degree of distortion from a perfectly tetragonal structure. This coefficient provides valuable information about the oxygen ordering and phase purity of the YBCO ceramic structures. It was calculated using Eq. (5), based on the previously determined lattice parameters a and b:

$$\delta = \frac{100(a-b)}{(a+b)} \tag{5}$$

A higher δ value typically reflects increased orthorhombic distortion, which may influence the superconducting properties of the YBCO ceramics. The combined crystallite sizes and orthorhombicity values display essential structural insights into the effects of Zn substitution on the Y-123 and Y-358 superconducting phases.

The surface morphology of the ceramic superconductor samples was examined scanning electron microscopy (SEM), with micrographs obtained at a magnification of × 10,000 using an FEI QUANTA FEQ 250 instrument. To evaluate the elemental composition and detect possible impurities, energy-dispersive X-ray spectroscopy (EDS) analysis was performed on selected localized regions of the ceramic structures. For EDS measurements, multiple point analyses were performed over different regions of each sample to minimize local compositional variations and improve statistical reliability. The averaged Zn contents follow the expected trend with increasing doping, even if absolute values may slightly deviate due to known EDS limitations. The electrical resistivity measurements were carried out in the temperature range of 10–300 K using the four-probe method within a Janis CCS-450 cryostat system, allowing for precise control of low-temperature conditions.

As noted earlier, the hole carrier concentration (P) per Cu ion is a key parameter governing electrical transport and superconducting behavior in cuprate ceramics. The relationship between the superconducting transition temperature and hole concentration follows a well-established nonlinear

trend, commonly described by a universal parabolic relation. The empirical model proposed by Presland et al. quantitatively captures this dependence [52, 53]:

$$\frac{T_c^{offset}}{T_c^{max}} = 1 - 82.6(P_{hole} - 0.16)^2 \quad (6)$$

where T_c^{offset} is the offset superconducting transition temperature of the sample, and T_c^{max} is the maximum transition temperature at the optimal doping level of $P_{hole} \approx 0.16$. This relation has been widely validated for Bi-, Y-, and Tl-based superconductors.

For the underdoped region of Bi-2212, the hole concentration in the valence band can be estimated using Eq. (7) [54, 55]:

$$P_{hole} = 0.16 - \left[\frac{\left(1 - \frac{T_c^{offset}}{T_c^{max}}\right)}{82.6}\right]^{\frac{1}{2}} \quad (7)$$

According to this framework, superconductivity reaches its maximum near optimal doping ($P_{hole} \approx 0.16$), while deviations toward either the underdoped or overdoped regimes result in a reduction of transition temperature [56]. This relation provides valuable information about the doping level and its influence on the electrical superconducting properties. Below the T_c parameter, materials contain superconducting electron pairs; however, superconducting behavior is not fully established until the T_c value is reached. These pairs give rise to superconducting fluctuations, caused by thermodynamic processes that intermittently form and annihilate electron pairs [57]. A deviation from linearity in the ρ–T curve above T_c serves as an indicator of such fluctuations.

The electronic properties of YBCO are strongly anisotropic in both the normal and superconducting states, and this anisotropy is experimentally observable. Due to their short coherence lengths and high anisotropies, high-temperature superconductors are well-suited for the detection of fluctuation-induced conductivity using the ρ–T graph [58]. The total fluctuation conductivity consists of two primary contributions, expressed as follows:

$$\Delta\sigma = \Delta\sigma^{AT} + \Delta\sigma^{MT} \quad (8)$$

where $\Delta\sigma^{AT}$ is the Aslamazov–Larkin (AL) fluctuation, and $\Delta\sigma^{MT}$ is the Maki–Thompson fluctuation. However, this model assumes homogeneity and is not directly applicable to polycrystalline samples. Therefore, Lawrence and Doniach (LD) extended the AL theory for layered copper-based superconductors, such as those containing weakly coupled copper oxide planes. The LD model, derived from AL theory, predicts a dimensional crossover from 2 to 3D fluctuations near T_c. In this framework, the fluctuation-induced conductivity is given by

$$\Delta\sigma_{LD} = A_x\varepsilon^{-1}\left[1 + \left(\frac{2\xi_C(0)}{d}\right)^2\varepsilon^{-1}\right]^{-\frac{1}{2}} \quad (9)$$

Here, $\xi_c(0)$ is the zero-temperature coherence length along the c-axis, d is the interlayer spacing, and ε is the reduced temperature, calculated using the relation:

$$\varepsilon = \frac{T - T_c^{mf}}{T_c^{mf}} \quad (10)$$

The system exhibits 3D fluctuations above the crossover temperature T_{LD} and 2D fluctuations below the temperature value. The crossover temperature is determined by

$$T_{LD} = T_c^{mf}\left[1 + \left(\frac{2\xi_C(0)}{d^2}\right)^2\right] \quad (11)$$

The experimental fluctuation conductivity is obtained from measured resistivity values and is given as in Eq. (12):

$$\Delta\sigma = \left(\frac{1}{\rho} - \frac{1}{\rho_n}\right) \quad (12)$$

where ρ is the measured resistivity and ρ_n is the normal-state resistivity, estimated from the linear portion of the ρ–T curve using Eq. (13):

$$\rho_n = \alpha + \beta T \quad (13)$$

Two critical parameters for analyzing fluctuation conductivity are the accurate determination of ρ_n and the mean-field critical temperature T_c^{mf}. The plot of $\ln(\sigma)$ versus $\ln(\varepsilon)$ reveals the fluctuation region, and the critical exponents λ_{2D} and λ_{3D} can be extracted from the slope of the linear regions. Furthermore, the zero-temperature coherence length $\xi_C(0)$ can be estimated from the value of T_{LD} derived from the $\ln(\sigma)$–$\ln(\varepsilon)$ plot [59, 60].

Magnetization measurements were carried out using a Lakeshore 7400-S model vibrating sample magnetometer to investigate the magnetic properties of the synthesized superconducting samples. All measurements were performed at a fixed temperature of 20 K under an applied external magnetic field ranging from − 2 T to + 2 T. The resulting magnetization versus magnetic field (*M–H*) curves were analyzed to determine the coercivity, remanent magnetization, and intragranular J_c values. These values were calculated using Bean's critical state model, as described by the following expression (Eq. (14)) [61], which assumes a uniform current distribution within the grains of the ceramic superconductor.

$$J_c(H) = 20\frac{\Delta M}{a\left(1-\frac{b}{3a}\right)} \tag{14}$$

The F_p is a key parameter in understanding the pinning mechanisms that govern the performance of superconductors under applied magnetic fields. To conduct a more comprehensive analysis of the pinning behavior, three theoretical models were employed. These models take into account factors such as the geometry of defects (e.g., point, linear, planar, or surface), the type of interaction involved (either core or magnetic), and the nature of the pinning nucleation centers (normal or superconductor). The experimentally obtained pinning force values for the ceramic structures were analyzed and interpreted by comparing them with these three theoretical frameworks, as described in Eqs. (15), (16), and (17) [62].

Δκ pinning:

$$f_p(b) = 3b^2\left(1-\frac{2b}{3}\right) \tag{15}$$

Normal point pinning:

$$f_p(b) = \frac{9}{4b}\left(1-\frac{b}{3}\right)^2 \tag{16}$$

Normal surface pinning:

$$f_p(b) = \frac{25}{16b^{\frac{1}{2}}\left(1-\frac{b}{5}\right)^2} \tag{17}$$

where $b = H/H_{max}, f_p(b) = F_p\big/F_{max}$.

3 Results and discussion

3.1 XRD measurements

This part includes the change of crystallinity quality, crystallite size, orthorhombic-to-tetragonal phase transition, grain orientation, texturing, and coupling strength between adjacent active Cu-O_2 layers for both the Zn/Cu-substituted Y-123 and Y-358 ceramic systems. XRD patterns of undoped and Zn-doped Y-123 superconducting samples are presented in Fig. 1. The diffraction peaks observed at high intensities correspond well with the standard orthorhombic Y-123 phase (Fig. 1a), as also verified by their respective Miller indices labeled on the patterns (Fig. 1b, c). No secondary phases, systematic peak shifts, or impurity peaks associated with Zn-doped Y-123 ceramic structures were detected, indicating that the Zn^{2+} ions were successfully incorporated into the Y-123 lattice without exceeding the solubility limit. The observed peak shifts further reveal slight variations in lattice parameters, arising from the ionic size difference between Zn^{2+} and Cu^{2+} ions, thus providing strong evidence of successful substitution. Moreover, Zn^{2+} ions are effectively incorporated into the host lattice, inducing controlled lattice distortions due to differences in ionic radius, electronic configuration, and electronegativity. The localized distortions are known to generate beneficial strain fields, promote slight lattice contraction, and enhance interatomic bonding within the defect-engineered matrix. In more detail, the ionic radius of Zn^{2+} (0.74 Å) is very close to that of Cu^{2+} (0.73 Å), which facilitates partial substitution at the Cu sites without significant lattice distortion. However, minor variations in peak intensities and positions were observed, especially in the sample with $x = 0.10$, which exhibited a slight rightward shift of the major diffraction peaks, implying localized strain or lattice contraction. The clear distinction between the (013)/(103) and (006)/(200) diffraction peaks, with the (006) peak possessing higher intensity, is a strong indication of the orthorhombic symmetry preserved in the crystal structure and sufficient oxygen content. The features confirm that the oxygen deficiency is minimal and the oxygen chains remain ordered, which is critical for the superconductivity phenomenon of YBCO ceramic structures. Lattice cell constants and crystallite size values, summarized in Table 1, further support the discussed scientific findings. Despite slight deviations from the ideal lattice constants reported in the

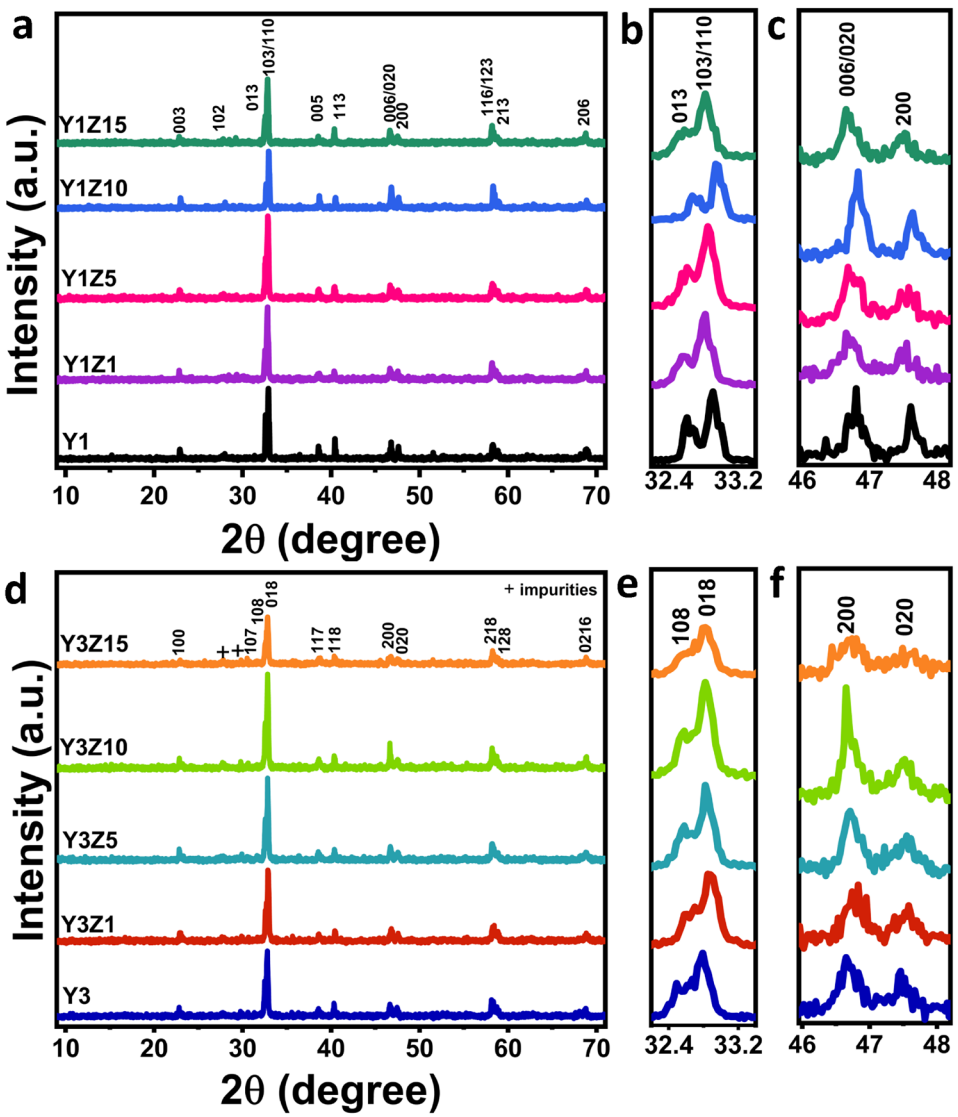


Fig. 1 XRD patterns of Zn-doped samples. **a** Y-123, **b** magnified view of the (013) and (103/110), **c** magnified view of the (006)/(020) and (200), **d** Y-358, **e** magnified view of the (108)–(018), and **f** magnified view of the (200)–(020). Symbols (+) denote minor impurity reflections

Table 1 Crystallite size and lattice cell parameters of the Zn-replaced Y-123 and Y-358 structures

Samples	*D* (nm)	a(Å)	b(Å)	c(Å)	V(Å^3)	δ
Y1	31.21	3.822	3.885	11.654	173.034	0.814
Y1Z1	31.48	3.822	3.902	11.668	174.031	1.032
Y1Z5	30.77	3.822	3.891	11.659	173.377	0.887
Y1Z10	28.49	3.818	3.876	11.642	172.264	0.759
Y1Z15	30.98	3.831	3.886	11.677	173.861	0.715
Y3	28.35	3.894	3.831	31.445	469.103	0.812
Y3Z1	29.89	3.880	3.822	31.615	468.814	0.749
Y3Z5	29.04	3.889	3.824	31.662	470.941	0.840
Y3Z10	28.13	3.894	3.827	31.409	468.010	0.872
Y3Z15	27.91	3.892	3.829	30.899	460.412	0.812

literature [27], all Zn/Cu partially substituted Y-123 ceramic samples retained orthorhombic symmetry. Among the investigated crystal systems, the composition with $x = 0.10$ exhibited the most pronounced structural modifications, characterized by a significant reduction in orthorhombicity ($\delta = 0.759$) and the smallest average crystallite size (28.49 nm). In contrast, the unsubstituted and lightly substituted ($x = 0.01$) Y-123 ceramics retained comparatively larger crystallite sizes of 31.21 and 31.48 nm, respectively, highlighting that excess Zn incorporation suppresses grain growth and promotes structural disorder. Furthermore, the unit cell volume displayed slight but systematic fluctuations as a function of Zn^{2+} ion content, dispalying subtle variations in lattice packing. A progressive decrease in δ with increasing Zn concentration (most notably at $x = 0.10$ and $x = 0.15$) verifies a gradual tendency toward tetragonal distortion. This evolution is likely associated with partial oxygen deficiency and/or rearrangements within the Cu–O chain sublattice, in line with previously reported behavior in Zn-substituted YBCO systems [43, 44]. Shortly, the presence of Zn impurity damages crystallinity quality, crystallite size, orthorhombic-to-tetragonal phase transition, grain orientation, texturing, and coupling strength between adjacent active Cu-O_2 layers of the Y-123 system.

Additionally, the XRD patterns of unreplaced and Zn/Cu partially substituted Y-358 superconductors are shown in Fig. 1d. Examination of the diffraction patterns via literature [26] indicates that all samples predominantly exhibit orthorhombic crystal structure characteristics. This is confirmed by the presence and clear separation of typical orthorhombic phase peaks, namely (108)–(018) and (200)–(020), as illustrated in Fig. 1e, f. However, a careful inspection reveals that the purity of the Y-358 superconducting phase decreases slightly with increasing Zn content, and minor impurity traces begin to emerge, especially for higher doping levels. Although no distinct impurity peaks or Zn-based secondary phases were observed with increasing Zn doping up to $x = 0.15$, slight impurities and possible secondary phase formation appeared, especially at the 15% doping level, confirming that Zn^{2+} ions mostly substituted for Cu^{2+} within the lattice; however, excess dopant may have led to minor structural distortions and slightly disrupted the phase purity. Similar to the Y-123 crystal lattice, the close ionic radii of Zn^{2+} and Cu^{2+} support Zn^{2+} substitution for Cu^{2+} in the Y-358 ceramic matrix. However, increasing Zn content caused a noticeable decrease in peak intensities, especially for $x = 0.15$, indicating reduced crystallinity and structural disorder. In this sample, the (108)–(018) and (200)–(020) peaks are nearly merged, verifying orthorhombic phase degradation. As shown in Table 1, variations in lattice parameters, unit cell volume, and δ reflect the structural changes based on the Zn doping level. All the new synthesized Y-358 ceramic samples maintain orthorhombic symmetry, with δ values ranging between 0.749 and 0.872. The $x = 0.10$ sample displayed the highest δ (0.872), indicating the most well-defined orthorhombic phase among the Zn-doped series. In contrast, the $x = 0.15$% Zn ions added Y-358 sample showed a reduction in c-axis lattice parameter (30.899 Å) and unit cell volume (460.412 $Å^3$), along with the smallest average crystallite size (27.91 nm), reflecting the cumulative effect of lattice strain, oxygen deficiency, and potential phase instability at higher doping levels, as noted above.

The variation in crystallite size with Zn content exhibits a non-monotonic trend. Compared to the undoped Y-358 sample (28.35 nm), the grain size initially increases slightly at low doping levels (29.89 nm at $x = 0.01$), reaches a peak at $x = 0.05$ (29.04 nm), and then decreases with further Zn substitution amount, indicating that the presence of excess Zn incorporation may inhibit grain growth and promote defect formation. Additionally, a slight shift of the main peaks toward higher angles was detected with increasing Zn content, implying a reduction in lattice spacing and possible compressive stress within the crystal structure. On this basis, the incorporation of Zn impurities deteriorates the crystallinity, disrupts grain orientation and texturing, and weakens the interlayer coupling strength between adjacent CuO_2 planes, thereby compromising the overall superconducting performance.

In conclusion, Zn doping in Y-358 samples successfully preserves the orthorhombic phase up to $x = 0.10$, while higher doping levels induce peak broadening, intensity suppression, and local structural distortions. The findings in Fig. 1 confirm that while Zn is accommodated in the Y-358 ceramic lattice by replacing Cu atoms, the solubility limit is approached at $x = 0.15$, beyond which crystallinity and structural uniformity are notably compromised.

Figure 1, directly comparing the XRD patterns of Y-123 and Y-358 ceramic samples, further emphasizes the difference in Zn solubility behavior between the two phases. At $x = 0.01$ and $x = 0.05$ substitution levels,

both Y-123 and Y-358 exhibited comparable peak intensities and clean diffraction patterns. However, at $x = 0.10$, the Y-358 phase showed stronger diffraction peaks than the Y-123 ceramic superconducting phase, displaying relatively better structural integrity at this level. This trend reversed at $x = 0.15$, with the Y-358 sample experiencing more severe peak suppression and potential impurity formation compared to the corresponding Y-123 sample. These results imply that while both superconducting phases can accommodate Zn^{2+} ions to a certain extent, the tolerance of the Y-358 lattice to Zn doping diminishes more rapidly at higher doping levels, possibly due to the complexity of its larger unit cell and multi-layered CuO_2 consecutively stacked layers. Zn doping up to 5% appears to enhance or maintain the crystallinity and orthorhombic symmetry in both Y-123 and Y-358 ceramic systems, with only minor variations in lattice parameters. The changes remain within the expected limits for substitutional doping and do not indicate a structural phase transition. Beyond this threshold, structural degradation becomes more pronounced, particularly in the Y-358 phase, as evidenced by diminished peak intensities, reduced crystallite sizes, and overlapping characteristic reflections (Table 1). These observations indicate that the solid solubility limit of Zn in both superconducting phases lies between 0.05 and 0.10, beyond which lattice strain, phase disorder, and microstructural inhomogeneity emerge, potentially deteriorating superconducting performance. This effect is especially critical for the Y-358 phase, which is known for its inherent structural instability and sensitivity to synthesis conditions such as temperature, oxygen partial pressure, and cation stoichiometry. The formation of secondary phases is commonly observed due to the difficulty in stabilizing stoichiometrically pure Y-358. In Zn-doped samples, minor impurity peaks between 26° and 30° display the formation of additional secondary phases, such as Y-211, $BaCuO_2$, $BaCO_3$, and unreacted Y-123, particularly at higher doping levels [63, 64]. These findings confirm that Zn incorporation into the Y-358 lattice becomes increasingly challenging with higher doping, often resulting in intergrowth with other YBCO phases and increased impurity formation. Nevertheless, although Zn incorporation induces local lattice distortions and secondary phase formation in the Y-358 structure, such effects remain relatively modest at low substitution levels but become significantly amplified once the solubility limit is approached or exceeded.

3.2 SEM and EDS analyses

The SEM micrographs of Zn-doped Y-123 samples are presented in Fig. 2. These images were obtained at a magnification of × 10,000 in order to investigate the grain structure, intergranular spacing, surface uniformity, microcrystalline orientation, grain boundaries, melting regions, porosity, defect structures, and particle size distributions of the samples. Upon examination of the SEM images, Zn doping was found to exert a complex influence on the microstructure of the YBCO ceramic samples. Figure 2 shows that at low doping levels (1%), the particle size is reduced compared to the pure sample, and porosity increases significantly. With intermediate Zn contents (5–10%), the grains become more irregular and poorly connected, exhibiting enhanced porosity and the appearance of microcracks, indicating a disruption in the sintering process and increased grain boundary disorder. Interestingly, at the highest doping level (15%), the microstructure exhibits partial recovery. The grains become relatively larger and more uniform, with a reduced density of pores and microcracks compared to the 10% sample. This indicates that the adverse effects of Zn-induced lattice distortion are partially alleviated, enabling grain reorganization and improved structural integrity relative to the 10% composition. This reversal may be attributed to Zn reaching its solubility limit within the YBCO lattice, beyond which it promotes the formation of Zn-based secondary phases. These secondary phases can act as a flux, enhancing local mass transport and facilitating grain growth, a phenomenon also reported in previous studies [43, 44]. Therefore, while moderate Zn doping deteriorates grain connectivity and promotes porosity, higher Zn content may alter the sintering dynamics in a way that locally supports grain coarsening. Consequently, Zn incorporation significantly affects the sintering kinetics and grain boundary integrity, with the most adverse effects on microstructural homogeneity observed around the 10% doping level. At the 15% substitution level, although partial improvements in grain morphology are observed, the concurrent formation of secondary phases and their detrimental influence on superconducting properties become increasingly significant and cannot be overlooked. The elemental distribution and compositional profiles of the Zn/Cu partially replaced Y-123 ceramics were examined by energy-dispersive X-ray spectroscopy (EDS), as illustrated in Fig. 2, with the corresponding quantitative

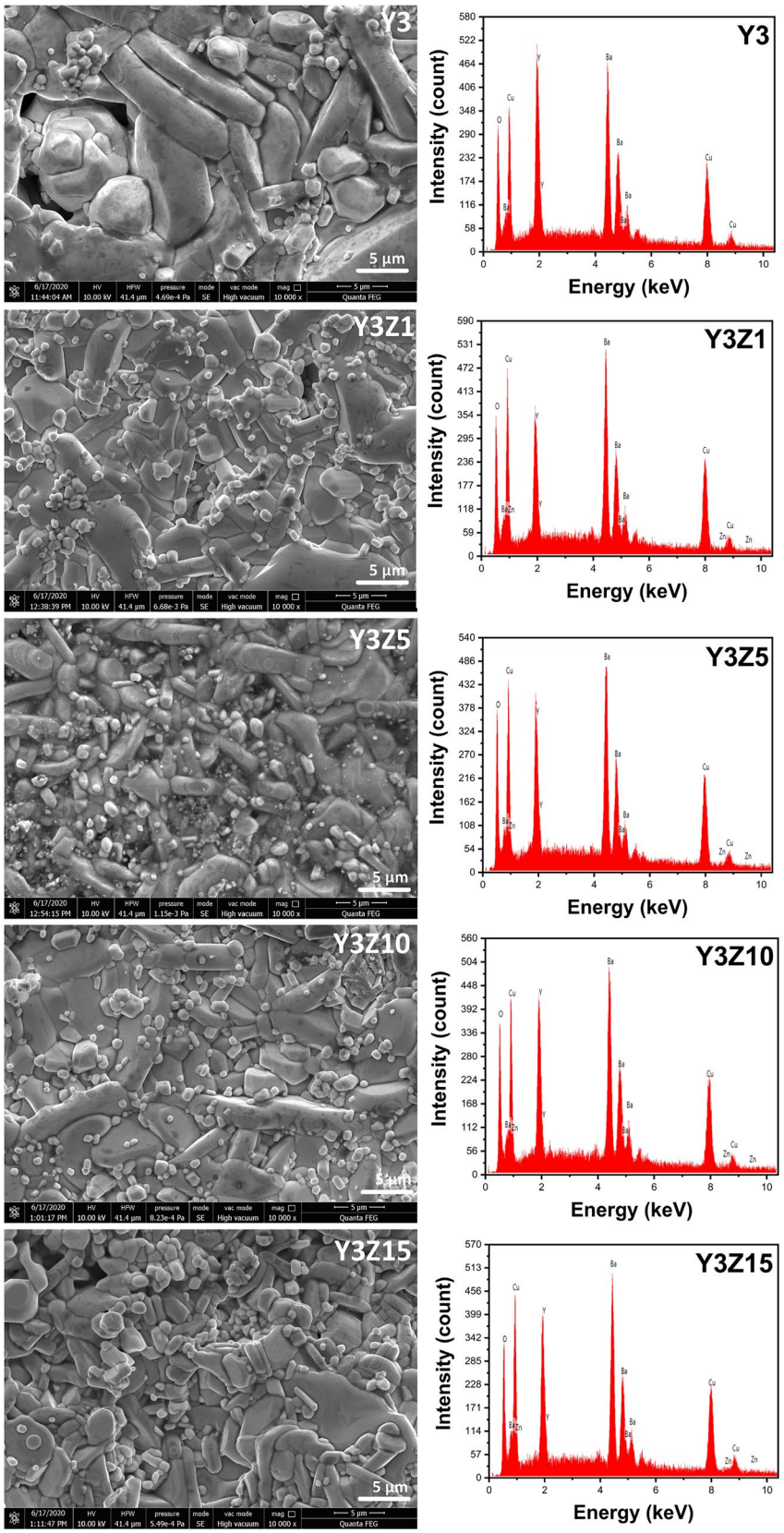


Fig. 2 SEM and EDS of the Zn-doped Y-123 and Y-358 samples

results summarized in Table 2. It is to be mentioned here that EDS technology has intrinsic limitations, particularly in quantifying light elements and providing highly precise stoichiometry. However, Zn is a relatively heavy element with a distinct X-ray emission line, which allows the Zn signal to be detected with reasonable sensitivity and accuracy compared to lighter elements along the experiments. Further, in the present study, EDS is not used as a standalone quantitative tool but rather as a complementary technique to verify the presence and relative distribution of Zn ions within the cuprate samples. The EDS analysis reveals a systematic increase in Zn concentration that correlates well with the nominal doping levels. This is because the EDS spectra performed consistently showed the presence of Zn peaks whose intensity systematically increases with the nominal doping level, indicating a clear correlation between intended and measured compositions. Concurrently, a proportional decrease in Cu content was detected, indicating a direct substitutional mechanism. In particular, it is found that the Zn weight fraction increased from 0.57 to 1.05%, while the Cu fraction decreased from 29.57 to 28.53%. This compositional trend provides strong evidence that Zn atoms occupy Cu lattice sites in the Y-123 crystal structure, consistent with the expected substitutional behavior. The compositional findings from EDS are strongly corroborated by structural and microstructural evidence.

Such substitutional doping is consistent with the hypothesis that Zn replaces Cu predominantly at the Cu^{2+} sites within the Cu-O_2 in-plane layers, which is known to affect both the superconducting and structural characteristics of the ceramic structure. The successful incorporation of Zn ions into the Y-123 superconducting phase, along with the reduction in Cu content, further supports the effectiveness of the sol–gel synthesis method in achieving controlled stoichiometry at the atomic level.

The SEM images of Zn-doped Y-358 samples are also shown in Fig. 2. The SEM micrographs clearly reveal that Zn doping significantly alters the surface morphology of the Y-358 ceramic samples. In particular, for the sample with $x = 0.15\%$ Zn doping, the grains appear smaller, more irregular in shape, and less oriented compared to those with lower doping levels. A noticeable degradation of the planar crystalline structure is evident, accompanied by particle agglomeration around the grain boundaries. As the Zn concentration increases, the grain alignment becomes increasingly disordered, displaying a disruption in the preferential growth direction of grains during the sintering process.

These morphological irregularities are indicative of the destabilizing influence of excess Zn ions on the crystal growth kinetics and indicate a limit beyond which Zn incorporation adversely affects the microstructural uniformity of the Y-358 superconducting phase formation. The observed porosity and disoriented grains at higher Zn levels may negatively impact the intergranular current transport by enhancing weak-link behavior.

Elemental compositions of Zn-doped Y-358 samples investigated by EDS analyses are presented in Fig. 2 and summarized in the accompanying data in Table 2. The EDS results confirm a systematic increase in Zn content with rising nominal doping levels, accompanied by a corresponding decrease in Cu content. This trend supports the substitutional incorporation of Zn^{2+} ions at Cu^{2+} sites within the Y-358 crystal lattice. For example, the sample with 1% Zn doping exhibited Zn and Cu weight percentages of 0.42 and 28.30%, respectively, whereas for the 0.15 doped sample, these values shifted to 1.46 and 27.28%.

The EDS data confirm effective Zn substitution at Cu sites up to the solubility limit and align well with the XRD and SEM results. Together, these results demonstrate that while low-to-moderate Zn doping supports lattice stability and compositional uniformity, excess doping near 15% induces localized phase instability and structural inhomogeneity, highlighting

Table 2 Local percent distributions of elements according to EDS analysis

Names	Weight %				
	O_K	Y_L	Ba_L	Cu_K	Zn_K
Y1	13.12	11.29	45.42	30.16	–
Y1Z1	11.61	10.41	47.84	29.57	0.57
Y1Z5	12.18	10.17	46.89	30.13	0.62
Y1Z10	13.4	9.13	47.63	28.88	0.97
Y1Z15	12.59	9.09	48.75	28.53	1.05
Y3	13.43	19.02	42.22	25.33	–
Y3Z1	12.73	13.46	45.09	28.3	0.42
Y3Z5	13.61	14.17	44.61	26.94	0.68
Y3Z10	12.94	14.68	44.25	27.25	0.88
Y3Z15	12.99	14.59	43.68	27.28	1.46

the critical importance of optimizing dopant levels for desired superconducting properties.

A comparative analysis of SEM and EDS results for Zn/Cu partially substituted Y-123 and Y-358 samples reveals distinct microstructural and compositional behaviors influenced by the doping level. In both phases, increasing Zn content leads to grain size reduction, enhanced porosity, and a disruption of grain boundary connectivity. However, the Y-358 ceramic sample exhibits a more pronounced morphological degradation, with a more porous and disoriented structure, particularly at 15% doping. The change of the main crystal structure is clearly seen from the other experimental results.

EDS findings consistently confirm Zn incorporation via Cu-site substitution, with a corresponding decrease in Cu content across both systems. Notably, while Y-123 shows partial microstructural recovery at high doping levels, Y-358 remains structurally unstable, indicating a lower tolerance for excess Zn ions. These observations highlight the critical role of phase-specific solubility limits and sintering dynamics in maintaining structural consistency and optimizing superconducting performance. At the same time, while EDS may not provide exact stoichiometric precision, it reliably confirms the presence, relative value, and homogeneous distribution of Zn in the samples. All these findings are consistent with other characterization experiments studied. When considered alongside the XRD, SEM, and EDS results, the combined evidence strongly confirms the successful attainment of the targeted substitution levels.

3.3 Resistivity measurements

The electrical transport characteristics of YBCO type-II superconductors are critically dependent on both extrinsic processing parameters (e.g., precursor purity, annealing conditions, mechanical strain, and dopant incorporation) and intrinsic microstructural factors, including the presence of microcracks, local lattice distortions, grain connectivity, and the interlayer coupling strength between adjacent CuO_2 planes. In the ceramic system, charge transport is predominantly mediated by mobile holes confined within the CuO_2 in-plane layers, which serve as the primary superconducting pathways. Consequently, any structural or compositional modification to these active planes, whether through oxygen stoichiometry variations, cation substitution, or induced strain, has a direct and profound impact on the electronic transport properties and fundamental superconducting performance of the ceramic matrix. The ρ–T behavior of Zn-doped Y-123 ceramic samples is shown in Fig. 3. It is observed from the figure that all samples demonstrated a clear superconducting transition, confirming that Zn substitution, even at higher doping levels, did not destroy the fundamental orthorhombic crystal structure required for superconductivity, having already been confirmed by XRD examinations. However, variations in Zn impurity content had a distinct and systematic effect on the superconducting properties. In detail, the Y1 sample exhibited a sharp and well-defined superconducting transition, with an onset temperature T_c^{onset} of 92.65 K and a narrow transition width $\Delta T_c = 2.65$ K.

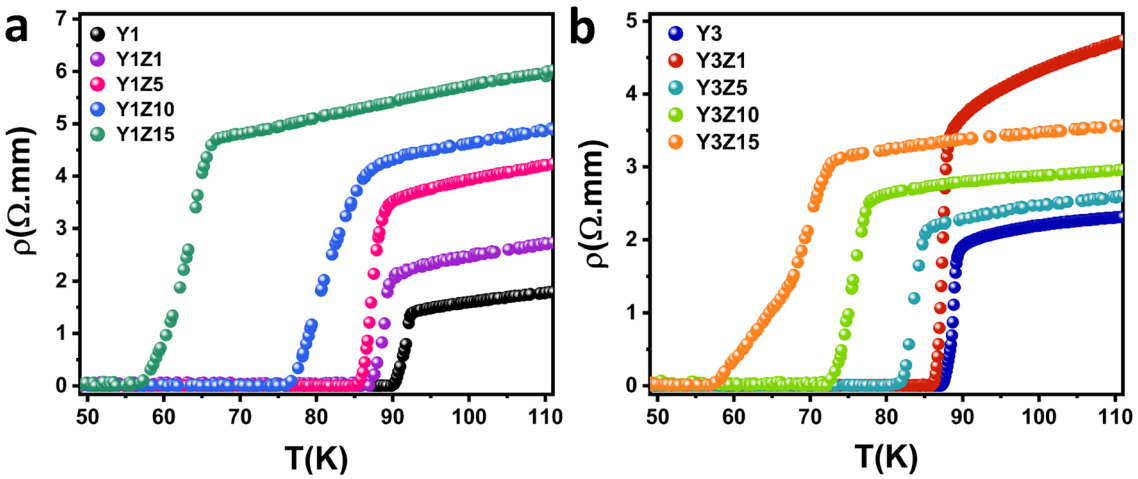


Fig. 3 Temperature-dependent electrical resistivity measurements of the Zn-doped **a** Y-123 and **b** Y-358 samples

This behavior is typical for high-quality Y-123 samples with minimal disorder and fine-grain connectivity. The Y1Z1 retained a similarly sharp transition ($\Delta T_c = 2.56$ K) and only a slight decrease in T_c^{onset} to 89.06 K, displaying that low-level Zn substitution may slightly disturb the superconducting network without significantly affecting phase homogeneity.

However, with increasing Zn concentration, a clear deterioration in superconducting properties was observed. For the Y1Z5 sample, the T_c^{onset} dropped to 88.79 K, while the transition width dramatically broadened to 12.84 K. This substantial increase in the ΔT_c parameter indicates increased structural inhomogeneity and the emergence of weak links between grains, likely due to Zn accumulation at grain boundaries, as evidenced by SEM observations.

Further doping to 10 and 15% Zn impurities caused a more pronounced suppression of superconductivity for the Y-123 superconducting phase. The onset temperatures decreased to 71.43 and 67.17 K, respectively, while the transition widths remained significantly large (7.32 for Y1Z10 and 10.72 K for Y1Z15). The transition curves in Fig. 3 also show that for the higher doping levels, the resistivity declines more gradually, indicating a less coherent, connected weak superconducting pathway. This phenomenon is typically associated with degraded crystallinity, reduced carrier density, and enhanced disorder at the microstructural level.

Additionally, the room-temperature resistivity (not quantified in the table but inferred from the ρ–T plots) was observed to increase with Zn content. This can be attributed to the scattering of charge carriers by Zn-induced defects and the reduction in short-range-ordered antiferromagnetic CuO_2 plane integrity, which impedes the charge transport necessary for both normal-state conductivity and superconducting pairing mechanism. Particularly in the 15% Zn-replaced sample, the electrical resistivity was markedly elevated, correlating with the most distorted microstructure and emergence of secondary phases despite partial improvements in grain morphology in SEM micrographs. This further confirms that excess Zn doping deteriorates the microstructure and increases scattering centers, hence reducing electrical conductivity and superconducting efficiency.

Consequently, similar to the XRD experiments, the electrical measurements confirm the detrimental effect of Zn substitution on superconductivity in the Y-123 superconducting phase beyond a certain threshold. While all Zn/Cu-substituted samples maintain superconducting behavior, Zn incorporation causes a progressive decrease in transition temperatures, a broadening of the transition width, and an increase in DC electrical resistivity. These effects are closely linked to Zn-induced microstructural disorder, reduced Cu-site availability, and weakened intergranular connectivity. It can therefore be concluded that Zn doping levels up to 1% are relatively tolerable within the Y-123 ceramic matrix, maintaining acceptable superconducting characteristics. However, higher doping levels, especially beyond 5%, introduce significant structural and electrical degradation, with 15% Zn doping severely affecting superconducting performance. This trend supports the identification of an optimal Zn content between 1 and 5% for balancing structural stability and superconducting efficiency in Zn-doped Y-123 materials. All in all, the excess Zn impurity impairs superconducting clusters stabilization, electronic bridges, localization of electronic density of states (DOS) at the Fermi energy level, and polaronic interactions in the strongly covalently bonded CuO_2 layers in the Y-123 ceramic structure.

As for the change of electrical and superconducting characteristics of Zn/Cu-substituted Y-358 ceramic structures, we depict the ρ–T experimental results in Fig. 3. It is obvious that every sample demonstrated superconducting transitions, indicating that the substitution of Zn impurity ions into the Y-358 crystal structure did not completely suppress superconductivity. However, the electrical transport measurements reveal a significant degradation in superconducting properties with increasing Zn content.

As shown in Table 3, the unsubstituted Y-358 ceramic structure exhibited a high T_c^{onset} of 90.01 K and a ΔT_c of 2.88 K, indicating good phase homogeneity and strong intergranular coupling. This clearly demonstrates the high structural and superconducting quality of the samples synthesized via the sol–gel method. In other words, the obtained ceramics exhibit enhanced grain connectivity, reduced porosity, and more uniform oxygen distribution, all of which are critical for achieving reliable superconducting pathways. These features not only validate the effectiveness of the sol–gel method in producing high-quality type II superconductors but also highlight its potential as a versatile synthesis technique for tailoring structural, electrical, and magnetic properties in complex oxide materials. However, as the Zn substitution level increased, the critical temperature gradually

Table 3 Characteristic parameters for the Zn/Cu-substituted Y-123 and Y-358 ceramic samples derived from ρ–T measurements

Samples	T_c^{onset}	T_c^{offset}	ΔT_c (K)	p
Y1	92.65	90.00	2.65	0.1438
Y1Z1	89.06	86.50	2.56	0.1331
Y1Z5	88.79	75.95	12.84	0.1140
Y1Z10	71.43	64.11	7.32	0.0994
Y1Z15	67.17	56.45	10.72	0.0916
Y3	90.01	87.13	2.88	0.1180
Y3Z1	89.68	84.99	4.69	0.1151
Y3Z5	85.57	80.63	4.94	0.1096
Y3Z10	78.97	71.87	7.10	0.1002
Y3Z15	73.88	56.98	16.90	0.0896

decreased. For instance, at 5% Zn substitution level, T_c^{onset} has decreased to 85.57 K, while ΔT_c slightly widened to 4.94 K. At 15% Zn doping, T_c^{onset} dropped significantly to 73.88 K, and ΔT_c increased dramatically to 16.90 K, revealing considerable inhomogeneity and weakening of the superconducting network. This widening of the transition region is indicative of Zn-induced disorder, which disrupts the connectivity of superconducting grains and weakens the coherence of the superconducting phase. Additionally, excess Zn incorporation detrimentally affects the stabilization of superconducting clusters, disrupts electronic bridging pathways, and enhances delocalization of DOS at the Fermi level. In addition, it interferes with polaronic interactions within the active Cu-O_2 planes of the Y-358 ceramic lattice, thereby undermining the intrinsic superconducting coherence of the system. Furthermore, in the ρ–T curve of the Y3Z15, a two-step transition behavior was observed due to the weak intergranular coupling, poor crystallinity, or the probable presence of Zn-rich non-superconducting regions at the grain boundary regions. Such structural features likely introduce energy barriers between superconducting grains, causing the superconducting transition to occur over an extended temperature range.

Additionally, the increase in normal state resistivity with Zn doping supports the presence of enhanced carrier scattering mechanisms. Zn atoms may substitute for Cu, primarily in the consecutively stacked CuO_2 planes, thereby possibly disrupting the superconducting charge transport pathways and reducing the mobile hole carrier concentration. This results in both suppressed superconductivity performance and degraded electrical conductivity. The greater sensitivity of the Y-358 superconducting phase to the Zn/Cu partial replacement mechanism, compared to the Y-123 phase, can be attributed to its more complex crystal structure and extended Cu–O networks, which may be more easily destabilized by aliovalent substitutions.

In summary, although Zn-doped Y-358 ceramic samples retain superconducting characteristics, their electrical transport properties degrade progressively with increasing Zn content. The observed reduction in T_c value, broadening of ΔT_c, increase in normal-state resistivity, and emergence of double-step transitions all point to structural and compositional inhomogeneities introduced by Zn impurity ions. These findings highlight the critical role of controlled doping in preserving superconducting performance, particularly in complex high-T_c phases like Y-358.

When compared with Zn-doped Y-123 ceramic structures, the bulk Y-358 samples exhibit a steeper decline in superconducting performance under the same replacement levels due to the considerable degradation in stabilization of superconducting clusters, electronic bridging pathways, and localization of DOS at the Fermi level. While both phases share a similar oxygen-dependent orthorhombic structure, the more complex and extended Cu–O chain and plane networks in the Y-358 ceramic structures appear more susceptible to structural disruption by the Zn/Cu substitution mechanism, where multi-phase cuprates were shown to be more vulnerable to doping-induced disorder due to their intricate crystal structure. While superconductivity is preserved at low Zn impurity levels, higher doping leads to significant deterioration in T_c parameters, increased ΔT_c, and signs of structural inhomogeneity. The sharp increase in transition width and the appearance of dual transition steps at 15% Zn doping highlight the importance of optimizing the Zn content for maintaining both microstructural integrity and superconducting functionality. For the Y-358 system synthesized, Zn doping levels above 5% appear to severely compromise superconducting coherence, rendering such compositions unsuitable for practical applications.

3.3.1 *Hole carrier concentration*

The charge carrier density is strongly governed by chemistry of the ceramic system, including charge

transfer dictated by the electronic band structure, the oxidation states of constituent ions, and the redox activity of metal atoms within the charge reservoir region. In this context, the hole-doping mechanism in the short-range-ordered antiferromagnetic CuO_2 planes is closely linked to cation vacancies, cationic substitutions, and the incorporation of excess oxygen. The hole concentration parameter of Zn-substituted Y-123 ceramic samples was quantitatively evaluated and is presented as a function of Zn substitution level in Fig. 4a, with the corresponding numerical values summarized in Table 3. The results reveal a parabolic decrease in carrier concentration with increasing Zn content, indicating that Zn substitution significantly affects the charge carrier density within the active CuO_2 planes. To illustrate, the Y1 exhibits a carrier concentration of 0.1438, which gradually decreases to 0.0916 in the Y1Z1 sample with the highest Zn/Cu replacement level of 15% Zn impurity ions. This reduction in p correlates closely with the observed suppression of the T_c, confirming that the decreased hole concentration in the CuO_2 planes adversely impacts superconducting properties.

The pronounced decline in carrier concentration beyond 5% Zn doping, where the ΔT_c significantly broadens, can be attributed to the disruption of electronic bridging pathways and orbital hybridization between copper and oxygen orbitals. The substitution of Zn^{2+} ions for Cu^{2+} introduces local lattice distortions and electronic inhomogeneities, which compromise the Cu–O orbital overlap essential for high hole mobility and superconducting pairing. Consequently, these lattice distortions lead to reduced electronic density of states at the Fermi level and impaired charge transfer mechanism within the superconducting planes.

Moreover, the rapid decrease in the p parameter with increasing Zn content displays that the stabilization of the crystal structure and the localization of electronic states are severely affected. This phenomenon likely arises from weakened interlayer coupling between adjacent superconducting planes and the formation of microscopic structural defects or dislocations. Such structural imperfections hinder coherent charge transport and facilitate carrier localization, further suppressing superconductivity.

In summary, the parabolic reduction in carrier concentration with increasing Zn/Cu partial substitution doping highlights the critical role of Zn impurity substitution in degrading the electronic environment of Y-123 ceramic superconductors. The observed correlation between decreased p values and lowered transition temperature supports the notion that maintaining optimal carrier density is essential for preserving superconducting performance, and that excess Zn doping induces detrimental effects through both structural disorder and electronic localization mechanisms.

In the Y-358 system shown in Fig. 4b and listed in Table 3, a similar decreasing trend in mobile hole carrier concentration is observed. The Y3 shows a p value of 0.1180, which drops to 0.0896 in the Y3Z15 ceramic structure. Although Zn^{2+} substitution introduces additional electrons into the system, the effect is a reduction in hole concentration. This paradoxical behavior is linked to enhanced oxygen uptake triggered by the

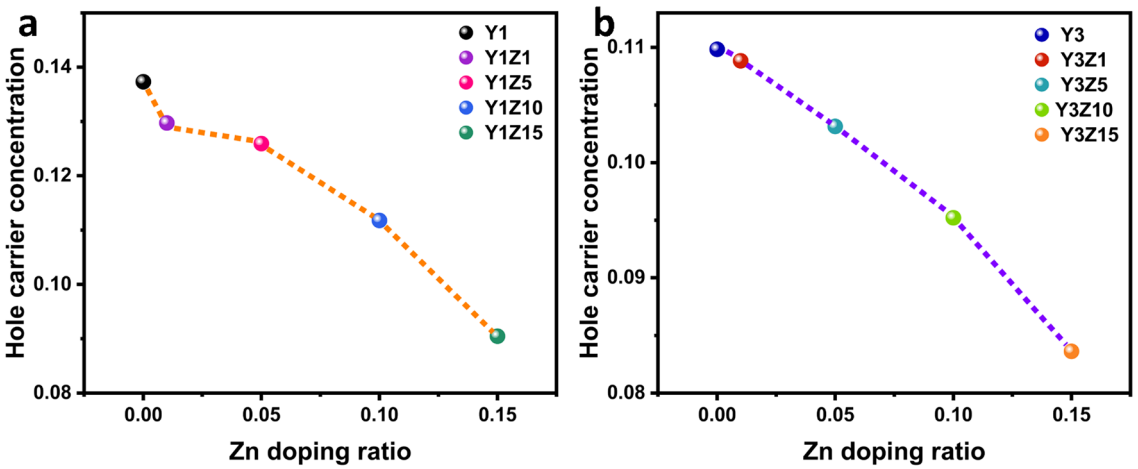


Fig. 4 Mobile hole carrier concentration values of the Zn-doped Y-123 and Y-358 samples

presence of excess electrons, which bind additional oxygen atoms within the lattice. The increase in oxygen content disrupts the optimum oxygen stoichiometry required for high-T_c superconductivity, resulting in a suppression of p and T_c parameters. Moreover, due to the difference in valence state, ionic radius, and electronic configuration between Zn^{2+} and Cu^{2+}, each substitution event introduces structural irregularities that hinder charge transport and coherence across the active CuO_2 planes.

While both Y-123 and Y-358 phases exhibit a decrease in mobile hole carrier concentration with increasing Zn content, the magnitude and nature of the reduction trend differ. The Y-123 system demonstrates a sharper parabolic decline in p values, especially beyond 5% Zn/Cu replacement level, highlighting its greater sensitivity to Cu-site substitution. In contrast, the Y-358 superconducting phase exhibits a comparatively more gradual decline in p parameter, which can be attributed to its structurally more complex framework that partially mitigates the detrimental effects of Zn-induced disorder. Nevertheless, in both crystal systems, Zn doping acts as an electron donor that disturbs the charge balance and structural stability of the CuO_2 stacked planes, leading to diminished hole concentration and a consequent suppression of superconducting properties. The critical threshold for pronounced degradation appears at ≥ 10% Zn content in both phases, where carrier localization and structural defects become dominant.

3.3.2 *Fluctuation-induced conductivity*

The fluctuation-induced conductivity analysis of Zn/Cu-substituted Y-123 phase was performed using $\ln(\sigma)$ vs. $\ln(\varepsilon)$ plots, as shown in Fig. 5. The linear region in these plots represents the mean fluctuation regime, from which the critical exponents λ_{2D} and λ_{3D} were determined based on the slope. Two linear fits were applied to identify the crossover behavior, and the intersection point was used to extract the corresponding dimensional transition temperature (T_{LD}) for each sample. The zero-temperature c-axis coherence length $\xi_C(0)$ was calculated using Eq. (10). Additionally, the mean-field critical temperature (T_c^{mf}) for each sample was extracted by extrapolating the normal-state resistivity curve and identifying the onset of superconducting fluctuations. The obtained values of T_c^{mf} (K), (T_{LD}), $\xi_C(0)$ (Å), (λ_{3D}), and (λ_{2D}) for all Y-123 ceramic samples are summarized in Table 4. It is obvious that the Y1 exhibited a high T_c^{mf} of 91.91 K and a crossover temperature (T_{LD}) of 115 K, characteristic of robust superconducting phase coherence and moderate fluctuation effects. The coherence length along the c-axis, $\xi_C(0)$, was found to be 0.97 Å, and the fluctuation exponents $\lambda_{3D} = 0.39$ and $\lambda_{2D} = 0.69$ indicate classical fluctuation behavior in cuprate superconductors, consistent with the quasi-two-dimensional nature of Y123 ceramic structure. In the Y1Z1 sample, a slight suppression of T_c^{mf} to 88.94 K and $\xi_C(0)$ to 0.82 Å was observed, while λ_{3D} and λ_{2D} remained close to those of the pristine sample, displaying minimal disruption to fluctuation dimensionality. However, even low-level Zn/Cu substitution amount appears to begin weakening interlayer coherence, as evidenced by the decrease in T_{LD} to a temperature value of 105 K. At Y1Z5 ceramic, λ_{3D} and λ_{2D} increased to 0.81 and 0.92, respectively, indicating enhanced thermal fluctuations, likely due to local inhomogeneities, delocalization of DOS at the Fermi level, and weak-link coupling behavior introduced by Zn at Cu sites in YBCO ceramic systems. Although $\xi_C(0)$ increased slightly to 0.90 Å and T_{LD} remained at 106 K, these values reflect a non-uniform superconducting state.

The effect becomes significantly more pronounced at higher Zn impurity levels. In the Y1Z10 sample, the parameter of T_c^{mf} dropped sharply to 80.03 K, while $\xi_C(0)$ decreased to 0.61 Å-indicating suppression of coherent interlayer coupling. Simultaneously, λ_{3D} and λ_{2D} rose dramatically to 1.91 and 3.23, respectively. Such high exponent values are indicative of a strong dimensional crossover from 3 to 2D fluctuation behavior, associated with disorder-driven decoupling of adjacent superconductive CuO_2 planes. For the Y1Z15 sample, T_c^{mf} further decreased to 63.46 K, accompanied by a low T_{LD} of 77 K. Interestingly, $\xi_C(0)$ recovered to 0.90 Å, which may indicate the emergence of filamentary or percolative superconductivity, and polaronic interactions within a highly disordered matrix. Nevertheless, elevated exponents ($\lambda_{3D} = 0.85$, $\lambda_{2D} = 1.84$) confirm that strong fluctuations and spatial inhomogeneities persist at this substitution level. Consequently, the fluctuation analysis reveals that increasing Zn content systematically degraded coherence of the superconducting phase and electronic bridging pathways, promoted dimensional decoupling, and enhanced fluctuation strength as much as possible. These trends are in line with theoretical models of impurity-related

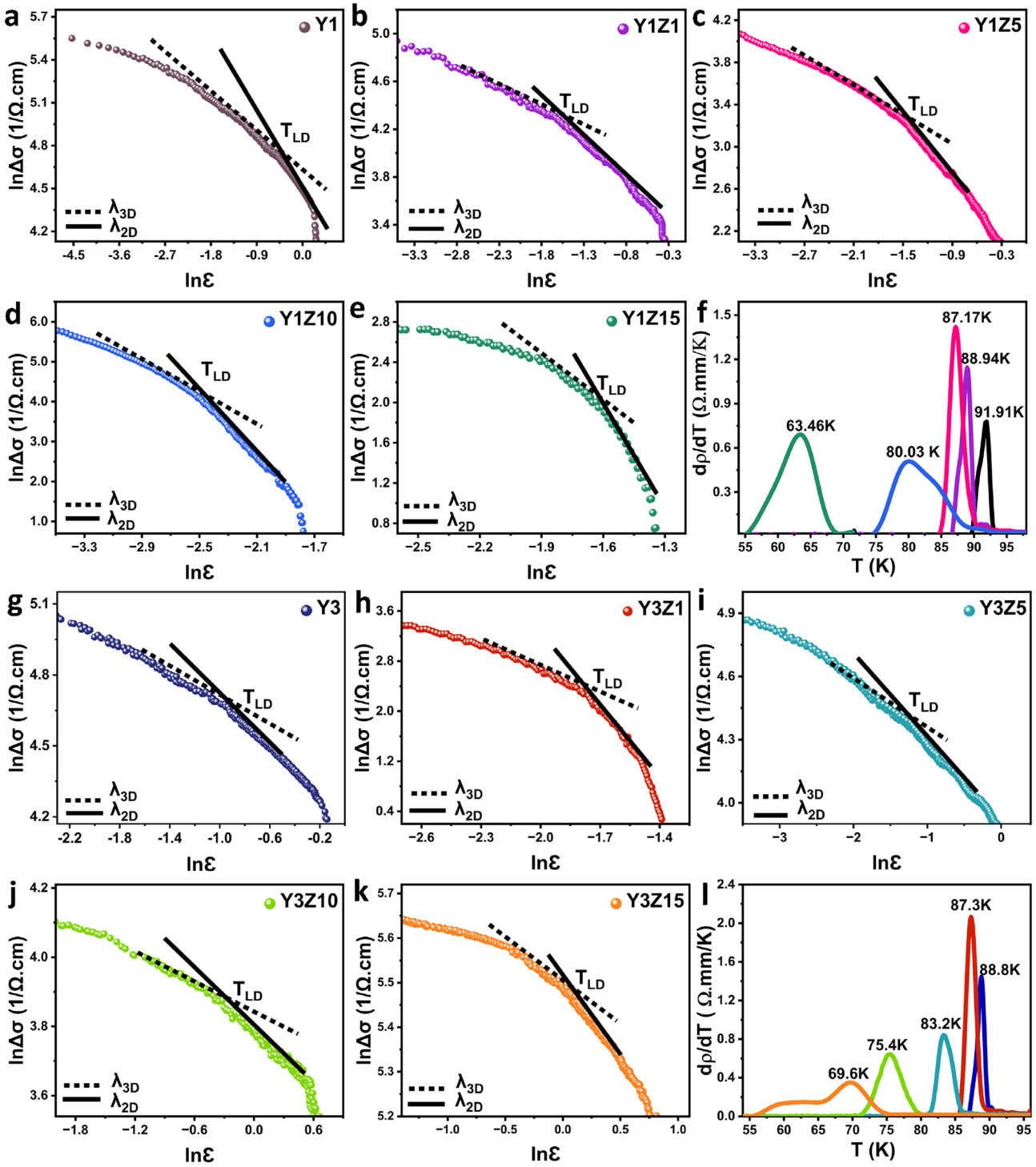


Fig. 5 Fluctiation-induced conductivity analyses of Zn-doped Y-123 and Y-358 samples

suppression of superconductivity in layered cuprates, reinforcing the role of Zn ions as a strong pair-breaker and disorder-inducing agent.

The fluctuation-induced conductivity parameters of Zn-substituted Y-358 ceramic samples, shown in Fig. 5 and listed in Table 4, reveal a relatively stable

Table 4 Characteristic parameters derived from the fluctuation-induced conductivity analyses of the Zn-doped Y-123 and Y-358 samples

Names	T_c^{mf}(K)	T_{LD}(K)	$\xi_C(0)$	λ_{3D}	λ_{2D}
Y1	91.91	115	0.97	0.39	0.69
Y1Z1	88.94	105	0.82	0.38	0.64
Y1Z5	87.17	106	0.90	0.81	0.92
Y1Z10	80.03	88	0.61	1.91	3.23
Y1Z15	63.46	77	0.90	0.85	1.84
Y3	88.87	106	0.88	0.46	0.88
Y3Z1	87.3	101	0.77	0.69	0.82
Y3Z5	83.2	105	0.99	0.72	0.84
Y3Z10	75.4	128	1.62	0.87	1.04
Y3Z15	69.6	142	1.98	0.91	1.20

fluctuation landscape, even under increasing Zn content. The undoped Y3 ceramic sample exhibits a mean-field transition temperature T_c^{mf} value of 88.87 K, a coherence length $\xi_C(0)$ of 0.88 Å, and moderate critical exponents ($\lambda_{3D} = 0.46$, $\lambda_{2D} = 0.88$), consistent with the expected quasi two-dimensional nature of the distorted oxygen deficient multi-layered perovskite structures.

Upon light Zn/Cu substitution (Y3Z1), T_c^{mf} slightly decreases to 87.3 K, and $\xi_C(0)$ drops to 0.77 Å, indicating the initial impact of Zn on interlayer coherence. Interestingly, both λ_{3D} (0.69) and λ_{2D} (0.82) increase, indicating a marginally stronger fluctuation regime even at low doping levels. At Y3Z5, the fluctuation regime appears to stabilize, as evidenced by an increase in $\xi_C(0)$ to 0.99 Å and relatively unchanged exponents ($\lambda_{3D} = 0.72$, $\lambda_{2D} = 0.84$). This is in attribution to the fact that the structural complexity of the Y-358 phase may buffer against Zn-induced disruption, maintaining interlayer coherence and preserving fluctuation dimensionality. On the contrary, more pronounced effects appear at higher Zn concentrations. In the Y3Z10 sample, $\xi_C(0)$ increases significantly to 1.62 Å, and T_{LD} sharply rises to 128 K, indicating an extended fluctuation regime and enhanced coherence along the *c*-axis length. The increased critical exponents ($\lambda_{3D} = 0.87$, $\lambda_{2D} = 1.04$) reflect stronger superconducting fluctuations, likely due to spatial inhomogeneities, delocalization of DOS at the Fermi level, and disorder-driven enhancement of phase fluctuations. This trend continues in the Y3Z15 sample, with $\xi_C(0)$ reaching 1.98 Å and T_{LD} further rising to 142 K. These unusually high values indicate the emergence of enhanced interlayer coherence, potentially arising from incoherent tunneling processes or proximity-induced coupling between superconducting clusters embedded within a structurally disordered matrix.

The critical exponents ($\lambda_{3D} = 0.91$, $\lambda_{2D} = 1.20$) remain elevated but do not display abrupt jumps, confirming that fluctuations strengthen progressively with impurity doping mechanism rather than abruptly transitioning between fluctuation regimes. Consequently, the findings observed indicate that the Y-358 structure maintains a robust fluctuation regime under Zn doping. The combination of increasing $\xi_C(0)$ and T_{LD} with slight alterations of λ exponents highlights the resilience of the Y-358 phase as a result of its extended chain and plane network, which helps preserve interlayer coupling and suppress severe fluctuation instabilities.

Fluctuation conductivity analysis further confirms that the Zn/Cu partial substitution mechanism induces a dimensional crossover and enhances superconducting fluctuation effects in both Y-123 and Y-358 superconducting phases, depending on the extent and nature of phase-dependent electronic anisotropy and coupling strength. While the Y-123 ceramic phase experiences a rapid suppression of coherence and pronounced two-dimensional fluctuation signatures beyond 5% Zn substitution, the Y-358 phase exhibits comparatively stable behavior characterized by an extended coherence length and more moderate fluctuation exponents. The observations recorded point out the decisive influence of crystallographic phase structure and interplanar coupling strength in governing fluctuation dynamics under chemical perturbation. From an application standpoint, the Y-358 architecture demonstrates superior tolerance to nonmagnetic impurity incorporation, such as Zn impurity, making it a more robust candidate for device technologies requiring precise control over superconducting fluctuations.

When comparing the effects of Zn/Cu substitution on the Y-123 and Y-358 superconducting phases, several key distinctions become evident. The Y-123 phase exhibits a more pronounced decrease in T_c^{mf} with increasing Zn content, whereas the Y-358 superconducting phase maintains relatively higher T_c^{mf} values, indicating stronger resistance to Zn-induced suppression of electron pairings into Cooper pairs in the conductive CuO_2 layers. In the Y-123 phase, a sharp reduction in $\xi_C(0)$ indicates significant disruption of *c*-axis coherence, while in Y-358 phase, $\xi_C(0)$ increases, likely

reflecting disorder-induced enhancement of coherence across larger inhomogeneous domains. Similarly, both λ_{3D} and λ_{2D} parameters rise rapidly in Y-123 phase but more gradually in Y-358 phase, revealing that Zn incorporation drives a stronger 3D–2D fluctuation crossover in the Y-123, whereas the Y-358 preserves a predominantly 3D-like fluctuation character due to its structurally stable framework. Consequently, Y-358 superconducting phase demonstrates superior dimensional fluctuation stability, broader fluctuation regimes, and more resilient coherence lengths, indicating its greater potential for applications requiring enhanced tolerance to thermal fluctuations and impurity-induced stress.

3.4 Magnetic measurements

3.4.1 Magnetization measurements

Figure 6a illustrates the *M–H* hysteresis loops for undoped and Zn-doped Y-123 ceramic samples, measured at 20 K under varying external magnetic fields ranging from − 2 T to + 2 T. The observed magnetic hysteresis loops provide critical information about the flux pinning characteristics, vortex lattice elasticity, magnetic irreversibility, coercivity, remanence, interlayer Josephson coupling, weak-link behavior at grain boundaries, and energy dissipation mechanisms arising from the thermally activated motion of discrete 2D pancake vortices within the investigated YBCO superconductors. These properties are directly associated with the material's ability to carry persistent currents and its fundamental superconducting performance under applied fields.

The undoped Y-123 sample displays the widest hysteresis loop, indicative of strong flux pinning and robust superconducting characteristics. The high magnetization values and broader loop area indicate a high J_c parameter, consistent with the expected behavior of well-ordered Y-123 systems. This pronounced magnetic irreversibility stems from effective pinning of magnetic flux lines, which are resisted in their motion by intrinsic defects and grain boundaries within the material matrix.

As the Zn/Cu substitution level increases from 1 to 15%, a progressive narrowing of the hysteresis loops is clearly evident. This narrowing reflects a systematic reduction in magnetization, implying a decrease in the pinning strength of flux vortices. The diminishing loop area directly indicates a weakening of the superconducting shielding currents, most likely due to the disruption of the active CuO_2 planes where superconductivity primarily resides. Zn ions, being a nonmagnetic and aliovalent ion, preferentially substitute for Cu^{2+} ions in the Cu-O_2 planes, hence introducing local electronic disorder and scattering centers that degrade the superconducting order parameter, forming electron pairings into Cooper pairs, and electronic bridging pathways. Such substitution disrupts the coherence of the superconducting pairs and reduces the effective density of states participating in the superconducting phase. Moreover, Zn substitution locally suppresses the superfluid density and weakens key superconducting interactions, including the effective pinning mechanism, interlayer Josephson

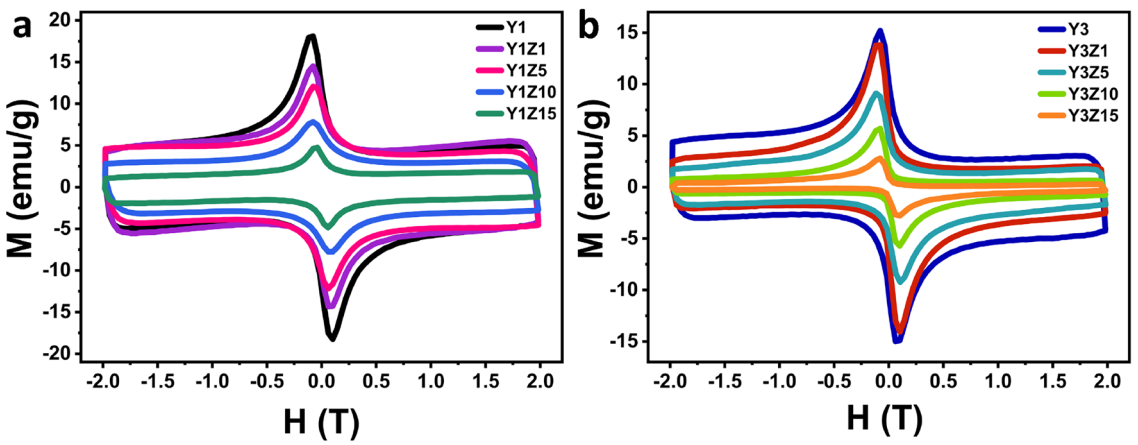


Fig. 6 Magnetization hysteresis loops of the Zn-doped Y-123 and Y-358 samples at 20 K

coupling, and vortex lattice elasticity. This facilitates vortex motion and results in a reduced diamagnetic response. Additionally, the suppression of superconducting parameters (T_c and J_c), along with increased disorder and microstructural degradation arising from Zn substitution at Cu sites, further supports the deterioration of the effective pinning mechanism and related phenomena. The reduction of the diamagnetic signal, as evidenced by the diminished magnetization values and loop widths, reveals that Zn/Cu partial substitution not only weakens flux pinning capability but also negatively affects the ability to expel magnetic flux.

The magnetization measurements under varying magnetic fields at 20 K clearly demonstrate that Zn doping has a deleterious effect on the flux pinning and magnetic performance of Y-123 superconductors. While low-level Zn doping causes moderate suppression, higher doping concentrations (≥ 10%) significantly deteriorate the superconducting magnetic response. These findings emphasize the delicate balance between structural stability and electronic coherence in high-T_c cuprate superconductors and highlight the critical role of CuO_2 plane consistency for maintaining durable superconducting and magnetic behavior.

The magnetization loops of undoped and Zn/Cu partially replaced Y-358 ceramic structures, shown in Fig. 6b, exhibit a clear trend in which the undoped sample shows the widest hysteresis, indicating robust magnetic irreversibility and strong vortex pinning. As Zn content increases, a gradual narrowing of the hysteresis width is observed. This decrease in loop area signifies a deterioration in the ability to pin magnetic vortices, which directly translates to a reduction in the critical current density. The maximum J_c values are achieved in the pristine Y-358 sample, while Zn-substituted samples exhibit consistently lower J_c values, particularly at higher fields.

This reduction in magnetic performance with Zn incorporation can be attributed to several microstructural and intrinsic modifications in the superconducting matrix. First, the substitution of nonmagnetic Zn^{2+} ions at Cu^{2+} sites within the CuO_2 planes and Cu–O chains disrupts the electronic environment and depletes the hole carrier concentration, weakening the superconducting order parameter, forming electron pairings into Cooper pairs, and creating electronic bridging pathways. Second, SEM analyses (as discussed in previous sections) have shown that the mechanism of Zn substitution leads to grain refinement, increased porosity, and structural disorder, especially at grain boundaries. All the changes observed weaken the intergranular interaction between grains and introduce non-superconducting phases or ineffective pinning regions, leading to enhanced flux creep and reduced pinning strength.

Furthermore, the decrease in hysteresis loop width and J_c values with increasing Zn content indicated that the flux pinning centers present in the undoped YBCO ceramic structure are either suppressed or rendered less effective by Zn incorporation. This could be due to a combination of disrupted oxygen stoichiometry and increased lattice distortions, which can negatively affect the formation and stability of intrinsic pinning nucleation centers. The intergranular Josephson coupling weakened, and the occurrence of weak-link behavior further increased. Consequently, Zn/Cu partial substitution is found to have a detrimental effect on the flux pinning properties and magnetization behavior of Y-358 superconductors at a temperature of 20 K. The observed decline in both J_c and hysteresis width indicates a compromised vortex immobilization capability, which is likely a consequence of altered microstructure, oxygen deficiency, and reduced coherence across the superconducting network. Therefore, while Zn substitution mechanism is often employed to investigate scattering effects and pseudogap behavior in high-T_c materials, its role in enhancing flux pinning in the Y-358 appears limited and counterproductive beyond a certain threshold.

Additionally, in Fig. 6a, b, the points where the magnetization curves intersect the H-axis correspond to the coercive fields. All samples display soft magnetic character due to nearly symmetrical hysteresis loops. For both Y-123 and Y-358 ceramic series, the unsubstituted ceramics (Y1 and Y3) exhibit the broadest loop widths and the largest coercivity values, reflecting stronger flux pinning centers, higher magnetic irreversibility, and superior superconducting integrity. In contrast, progressive Zn doping leads to a systematic narrowing of the hysteresis loops, with a pronounced decrease in coercivity as Zn/Cu replacement impurity concentration increases. This reduction is attributed to enhanced structural and electronic disorder, which weakens vortex pinning capability and reduces the ability of the superconducting grains to sustain trapped flux under applied fields. Similarly, the pristine samples also exhibit the highest remanent magnetization, consistent with stronger persistent supercurrents and strong intergranular coupling

character. As Zn content increases in the crystal lattice, the remanence decreases monotonically, reaching minimum values at the highest substitution levels. Among the substituted ceramic groups, the YZ15 sample, in particular, demonstrates markedly reduced coercivity and remanence, confirming a substantial suppression of flux pinning efficiency, vortex lattice elasticity, interlayer Josephson coupling, and electrical superconducting performance.

3.4.2 Critical current density

Figure 7a (extracted from *M–H* hysteresis loops) presents the variation of J_c parameters as a function of external magnetic field for undoped and Zn-doped Y-123 ceramic structures at 20 K. The J_c values were calculated from the magnetic hysteresis data using Bean's critical state model (relating the magnetic moment hysteresis width to the critical current density in type II superconductors). The model assumes a slab-like geometry where the magnetic field is applied parallel to the thickness (*c*-direction) of rectangular prism-shaped samples having a surface area ($a \times b$). This orientation allows for reliable estimation of J_c values, accounting for the sample dimensions and magnetization loop width (ΔM).

The solid Y1 ceramic structure exhibits the highest J_c values over the entire field range, starting at over 30 kA/cm^2 in the self-field (near 0 T) and gradually decreasing with increasing magnetic field strength. This behavior is consistent with strong vortex pinning and a well-preserved superconducting structure, supporting high current densities by impeding flux motion effectively. With Zn/Cu substitution, a noticeable and systematic suppression in J_c is observed. At the lowest doping level (when $x = 0.01$), the reduction in J_c is modest, indicating minimal disruption to the superconducting pathways. However, as the Zn content increases to higher substitution levels of $x = 0.05$, 0.10, and ultimately 0.15, the critical current density decreases progressively. For the highest Zn-doped sample ($x = 0.15$), J_c falls below 10 kA/cm^2 even at low fields, indicating significant degradation in flux pinning capability. The decline in J_c values with Zn doping is attributed to the substitution of Zn^{2+} ions for Cu^{2+} ions in the CuO_2 planes, which are critical to the superconducting mechanism. Spinless Zn^{2+} ions, being nonmagnetic and acting as a strong scatterer, introduce a pair-breaking effect and disrupt the supercurrent-carrying channels along the crystal systems [65, 66]. The substitution leads to enhanced quasiparticle scattering, local suppression of the superconducting order parameter, and a reduction in the effective carrier density. These factors collectively contribute to a diminished pinning force and increased mobility of vortices, resulting in lower J_c values. In the Y-358 structure, where superconductivity relies on more complex interplane coherence, this disruption is more detrimental than in the Y-123 superconducting phase. As a result, it is

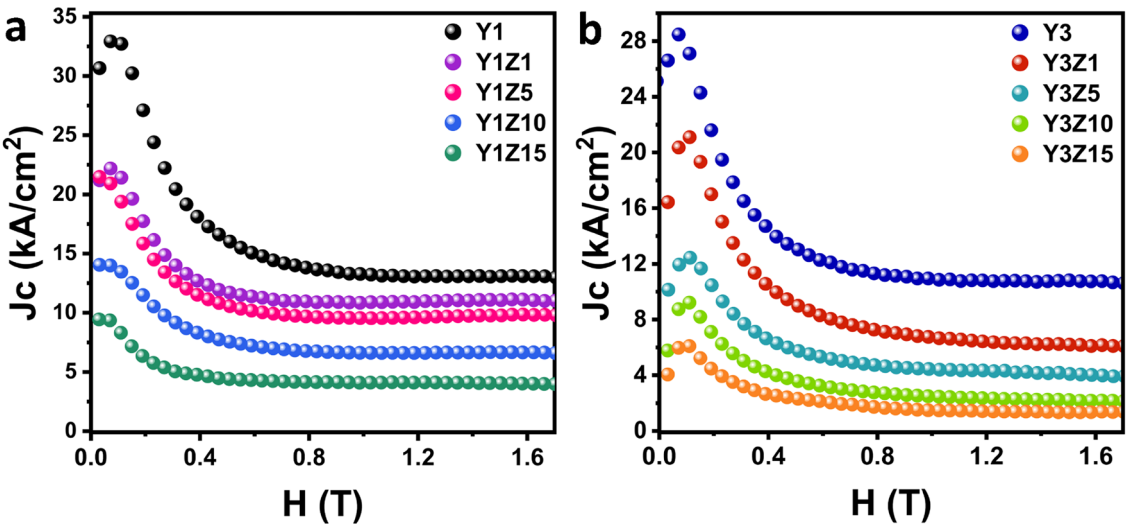


Fig. 7 Critical current density of the Zn-doped Y-123 and Y-358 samples

anticipated that even small amounts of Zn lead to a more pronounced degradation of superconducting and structural properties in Y-358.

Moreover, the rate of J_c suppression with field is also higher in Zn-doped YBCO ceramics compared to the undoped one, further supporting the interpretation that vortex motion is less hindered in the presence of Zn-induced defects. While low-level Zn substitution ($x \leq 0.01$) may introduce point-like pinning centers that slightly influence J_c, higher Zn concentrations markedly deteriorate the microstructural connectivity and homogeneity of the superconducting matrix.

Additionally, one can see the J_c behavior of Y-358 superconductors as a function of Zn doping in Fig. 7b. It is seen that low Zn doping adversely affects the current-carrying capability of Y-358 ceramic samples. A systematic decrease in the J_c parameter is observed with increasing Zn content, and this suppression trend becomes particularly pronounced beyond the 5% replacement level. For low Zn doping concentrations ($x \leq 0.05$), the decrease in J_c is relatively moderate, indicating partial retention of superconducting connectivity and pinning efficacy. However, at higher Zn levels ($x \geq 0.075$), a significant degradation in J_c values occurs, indicating that the microstructural and electronic disruptions induced by Zn^{2+} ion substitution reach a critical threshold beyond which the superconducting performance deteriorates rapidly. This decline in the J_c parameter can be attributed to several factors. Firstly, the substitution of Cu^{2+} with nonmagnetic Zn^{2+} ions in both the CuO_2 planes and Cu–O chains disrupts the local superconducting coherence and reduces the hole carrier concentration, thereby weakening the superconducting order parameter and forming electron pairings into Cooper pairs along the Y-358 crystal system. Secondly, the presences of Zn^{2+} ions induce grain refinement, widen grain boundaries, and increase porosity, all of which diminish intergranular coupling and form weak links across the superconducting matrix. The structural imperfections appeared reduce the current path continuity and facilitate vortex motion, further suppressing J_c parameters.

The sharp drop in J_c beyond 5% Zn/Cu substitution indicates that the superconducting network's ability to support persistent current is severely compromised, indicating that excessive Zn incorporation leads to a critical level of lattice and grain boundary disorder, oxygen deficiency, and intergranular decoupling. Consequently, the effective pinning volume and connectivity between superconducting domains are reduced, resulting in increased flux creep and lowered critical current.

While low levels of Zn substitution may be tolerated to some extent, excess doping (> 5%) is detrimental to the superconducting transport properties of the Y-358 phase. These findings highlight the importance of optimizing dopant concentration to maintain the balance between microstructural integrity and superconducting functionality. When all results are considered collectively, the relatively simpler structure of the Y-123 structure, along with more effective charge compensation via Cu–O chains and lower susceptibility to interlayer distortion, enables it to tolerate Zn substitution more effectively than the Y-358 superconducting phase. For practical applications where high J_c values are required, Zn doping in the Y-358 superconducting phase should be carefully controlled to avoid degradation of superconducting performance.

3.4.3 *Pinning force mechanism*

Figure 8a (inferred from *M–H* hysteresis loops) presents the magnetic field dependence of the F_p for undoped and Zn-doped superconducting Y-123 ceramic structures at 20 K. The undoped Y-123 sample exhibits the highest F_p values across the measured magnetic field range, indicating strong intrinsic flux pinning. As the Zn content increases from 1 to 15%, a clear and systematic decrease in the maximum F_p value is observed, indicating a degradation of flux pinning capability within the crystal system. Zn substitution is known to preferentially occur at Cu sites within the CuO_2 in-plane layers, which are the primary superconducting planes responsible for current transport and vortex pinning behavior. However, instead of forming artificial pinning centers, Zn acts as a source of disorder that disrupts the superconducting coherence length and weakens intragranular connections between grains, as discussed in previous sections in detail. The degradation of grain connectivity, coupled with microstructural inhomogeneity and the potential formation of secondary phases or defects, leads to a reduction in both the number and effectiveness of pinning centers.

To further clarify the nature of the vortex pinning mechanism in undoped and Zn-doped Y-123 superconducting series, the normalized pinning force F_p/F_{pmax} was analyzed as a function of reduced magnetic field, $h = H/H_{irr}$. The shape and peak position of

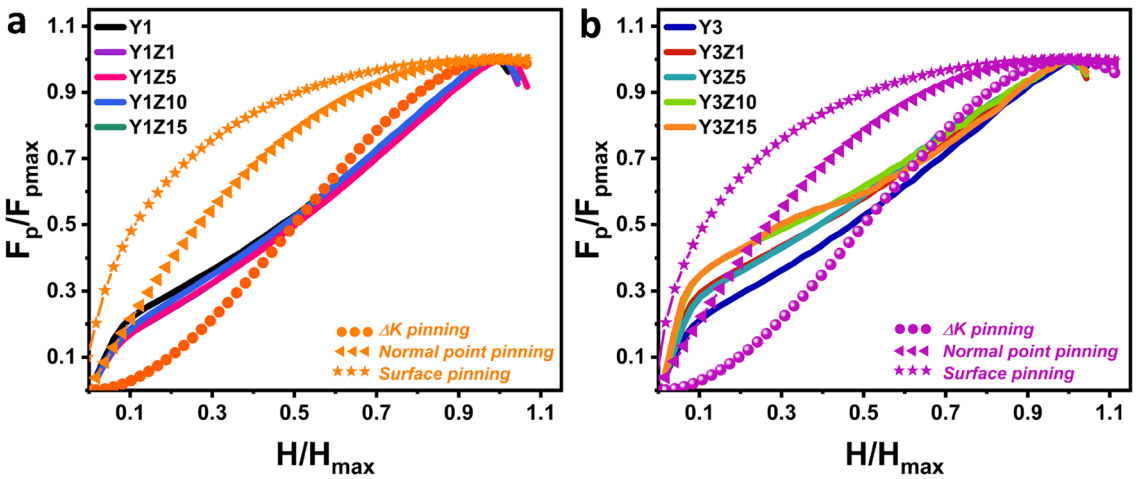


Fig. 8 Magnetic field dependencies of flux pinning force density for the Zn-doped Y-123 and Y-358 samples at 20 K

these normalized curves were compared to theoretical pinning models, such as normal point pinning, surface pinning, and spatial fluctuations in the Ginzburg–Landau parameter κ.

The experimental data for all samples exhibit the best correlation with the $\Delta\kappa$-type pinning model (based on qualitative interpretation of the superconducting and microstructural evolution), characterized by a normalized pinning force peak at $h = 0.33$, in excellent agreement with theoretical expectations for this mechanism. The $\Delta\kappa$ pinning behavior originates from local fluctuations in superconducting parameters, such as coherence length and critical temperature, typically caused by point defects, oxygen nonstoichiometry, or compositional inhomogeneities introduced during synthesis.

Zn doping in Y-123 introduces such compositional disorder by substituting Cu atoms in the CuO_2 planes, where superconductivity originates in the system. The substitutions disturb the uniformity of the superconducting order parameter and related mechanisms, leading to a non-uniform spatial distribution of κ. The observed alignment of the experimental curves with the $\Delta\kappa$ model confirms that the dominant pinning centers are not structural in nature (e.g., grain boundaries or secondary phases), but rather electronic or nanoscale defects arising from chemical inhomogeneity.

Moreover, the close matching between the experimental curves and the $\Delta\kappa$ model further indicates that Zn doping does not introduce effective strong pinning centers, such as those associated with dislocations, twin boundaries, or precipitates. Instead, the substitution mechanism degrades the superconducting matrix by weakening intergranular connections and enhancing flux creep, both of which lead to reduced pinning effectiveness.

Thus, while the undoped Y-123 ceramic structure exhibits relatively strong pinning and retains a more robust vortex lattice, the progressive replacement of Zn ions for Cu atoms reduces the effective flux pinning force and shifts the pinning mechanism toward a weaker, $\Delta\kappa$-type response.

The flux pinning data for Zn-doped Y-358 superconductors, presented in Fig. 8, exhibit a pronounced decrease in F_p values with increasing Zn content, indicating that the material's ability to effectively anchor magnetic vortices deteriorates markedly upon substitution. This behavior aligns with prior findings that substitution of Cu with Zn ions in high-T_c superconductors often leads to structural disorder, suppression of superconductivity, and a breakdown in intergranular coupling. Zn^{2+}, being a nonmagnetic ion, tends to disrupt the superconducting order and related characteristics without enhancing flux pinning as strongly as other dopants such as rare earths or nanoparticles, which can produce more effective nanoscale inhomogeneities. The observed reduction in grain size and the widening of grain boundaries in the doped samples, as evidenced by SEM micrographs, likely facilitate the formation of weak intergranular links and enhanced interfacial flux motion, thereby further degrading the overall flux pinning performance.

In Fig. 8b, the normalized pinning force density F_{pmax} is plotted as a function of h and compared with theoretical pinning models. At low magnetic fields, the experimental data for all Zn-doped ceramic structures show a behavior consistent with the normal point pinning mechanism, where isolated nanoscale defects locally trap vortices. However, as the applied magnetic field increases, the peak in F_p shifts toward higher h values, and the functional form becomes more compatible with the $\Delta\kappa$-type pinning model, where pinning is associated with spatial fluctuations in the Ginzburg–Landau parameter κ due to structural inhomogeneities.

The shift in dominant pinning mechanism with field strength indicates a complex interplay between microstructural disorder introduced by Zn impurity and the vortex dynamics. While at low fields isolated weak pinning centers dominate, at higher fields, the collective influence of disordered regions alters the pinning centers toward a $\Delta\kappa$-like regime. This duality is similar to observations in other Y-based systems with low-density or poorly distributed pinning centers.

Moreover, the lack of ability of Zn ions to form strong, coherent pinning centers is evident from the decrease of the maximum value of F_p and its shift in field dependence compared to YBCO ceramic samples doped with more effective pinning agents. This further supports the conclusion that, although Zn effectively modulates carrier concentration, it does not enhance vortex pinning in the Y-358 superconducting phase, particularly at higher doping levels.

Finally, comparative magnetic analysis of Zn/Cu partially replaced YBCO ceramic samples shows that the magnetic characterization of Zn-doped Y-123 and Y-358 superconductors provides a detailed understanding of how Zn incorporation influences flux pinning, magnetization behavior, and current-carrying capacity. Across both superconducting systems, doping levels of 1, 5, 10, and 15% Zn at the Cu site were systematically studied at 20 K. The results reveal a phase-dependent sensitivity to Zn impurity content, with the Y-358 structure showing more pronounced deterioration in superconducting performance beyond 5% Zn, as compared to the Y-123 superconducting phase.

The M–H hysteresis loops of both Y-123 and Y-358 ceramic structures revealed a progressive shrinkage in loop width with increasing Zn content. This behavior is indicative of a reduction in the trapped magnetic flux, implying weaker vortex pinning capabilities. The decline in the absolute magnetization values for both ceramic systems is directly linked to the reduction of superconducting volume and intergrain connectivity between the superconducting grains. Notably, the reduction is more pronounced in Y-358, displaying a higher structural sensitivity to the Zn doping mechanism, possibly due to its more complex crystallographic structure.

The J_c parameter exhibits a parabolic dependence on Zn impurity content for both superconducting phases. In the Y-123 ceramic structure, the value of J_c remains relatively stable up to 5% Zn, beyond which a pronounced decline occurs, marking a compositional threshold where Zn transitions from acting as a potential flux pinning center enhancer to primarily functioning as a scattering and pair-breaking center. In contrast, the Y-358 phase displays greater sensitivity to Zn incorporation, with even low-level doping (x = 0.01) causing a discernible suppression in J_c, followed by severe degradation beyond 5% Zn. This behavior verifies a more fragile pinning mechanism in the Y-358 superconducting phase, where microstructural disorder dominates over beneficial pinning effects. Supporting SEM analyses reveal reduced grain size, increased porosity, and widened grain boundaries with increasing Zn content, which collectively promote weak-link formation and intergranular decoupling, thereby further impairing the flux pinning and current-carrying capacity.

Flux pinning behavior, as represented by the pinning force density F_p, revealed crucial differences between Y-123 and Y-358 ceramic structures. For both ceramic systems, F_p decreased systematically with increasing Zn impurity content, with the effect more substantial in the Y-358 superconducting phase. The declining trend is aligned with previous reports indicating that Zn^{2+}, a nonmagnetic ion, lacks the capability to form strong pinning centers. Instead of reinforcing the flux pinning mechanism, Zn appears to introduce structural disorder, disrupting vortex confinement and leading to easier vortex motion under applied fields [43].

The normalized pinning force curves (F_p/F_{pmax} vs. h) for both Y-123 and Y-358 phases were analyzed and compared with Dew-Hughes' theoretical pinning models. On this basis, the assignment of pinning types is not derived from a rigorous model-based decomposition. Instead, the interpretation relies on established physical considerations and indirect experimental indicators. At low magnetic fields, both systems exhibit

behavior characteristic of normal point pinning, indicating the dominance of isolated defect-induced vortex dynamics. However, as the field strength magnitude increases, the curves progressively shift toward $\Delta\kappa$-type pinning, which is attributed to spatial fluctuations in the Ginzburg–Landau parameter (κ) arising from structural or compositional inhomogeneities. This observed crossover from point to $\Delta\kappa$-type pinning reflects the evolution of an inhomogeneous microstructure, a conclusion further supported by SEM observations, which reveal the presence of grain boundary disorder and non-uniform defect distributions with increasing Zn doping along the YBCO crystal systems. Interestingly, the Y-123 superconducting phase maintained a more coherent and stable pinning profile across all Zn doping levels, displaying that its relatively simpler crystal structure provides greater tolerance against Zn-induced disorder. In contrast, the Y-358 matrix, owing to its higher Cu and Ba content and more complex structural framework, exhibits enhanced susceptibility to interlayer decoupling and local suppression of superconductivity under similar doping conditions.

4 Conclusion

This work demonstrates the reliability and versatility of the sol–gel technique in synthesizing high-quality Type II ceramic superconductors. More importantly, it provides a detailed understanding of how Zn/Cu substitution alters the structural, electronic, and superconducting characteristics of Y-123 and Y-358 phases. These insights shed light on the fundamental mechanisms governing charge transport, vortex dynamics, and interlayer coupling in cuprate systems, while simultaneously offering valuable guidance for tailoring high-T_c materials toward advanced applications in superconducting electronics, energy storage, and high-field technologies. This work, based on controlled impurity engineering, will help us tune the functional properties in copper oxide superconductors. The scientific outcomes obtained from the study are as follows.

- XRD analysis confirmed the successful incorporation of Zn into the crystal lattices without the formation of prominent secondary phases at low doping levels, while minor impurity peaks appeared at higher Zn contents in the Y-358 samples. Both systems retained the orthorhombic structure at low Zn concentrations (≤ 5%), with minimal impurity formation and well-defined grains. However, Y-358 displayed a stronger sensitivity to the Zn doping mechanism, exhibiting pronounced peak suppression, reduced crystallite size, increased porosity, and structural disorder at higher Zn levels (> 5%).
- SEM and EDS results revealed that moderate Zn doping disrupted grain connectivity and increased porosity in both phases, whereas excessive doping (15%) led to partial recovery in grain morphology in the Y-123 ceramic structures due to the solubility limit, and with a stronger effect in the Y-358 phase, which likely influenced charge carrier mobility.
- Electrical measurements showed that increasing Zn concentration suppressed the T_c, broadened the ΔT_c, and reduced hole carrier concentration, driving the system into the underdoped regime. These changes were attributed to enhanced structural disorder and increased scattering centers. While low-to-moderate doping levels maintained reasonable phase purity and lattice stability, higher Zn content introduced microstructural inhomogeneity and adversely affected superconducting performance. Notably, Y-358 samples were more sensitive to Zn doping as a result of their more complex and metastable structure. Moreover, the degradation in Y-358 ceramics occurred more gradually, indicating that its complex lattice framework provides an intrinsic buffering effect against the initial perturbations introduced by Zn doping. Fluctuation conductivity analysis revealed that Y-123 experienced a sharper 3D–2D crossover, whereas Y-358 maintained broader fluctuation regimes and more resilient coherence lengths.
- The magnetic hysteresis results also show that Zn doping progressively narrows the loops and reduces coercivity and remanence, indicating weakened flux pinning, reduced vortex lattice elasticity, and diminished superconducting integrity. The Y-123 phase demonstrates greater tolerance to Zn substitution up to 5% without pronounced degradation in magnetic performance, whereas the Y-358 phase exhibits significant sensitivity even at low Zn concentrations. Both systems show a transition from point-type to Δκ-type pinning with increasing field strength; however, this crossover occurs more abruptly and is more structurally driven in Y-358. Magnetic and critical current measurements further confirm that flux pinning in Y-123 remains more

resilient, while Y-358 experiences a steeper decline in pinning efficiency and J_c, particularly beyond Zn ≥ 10%.

- Zn doping reduces p in both systems, correlating with the observed T_c suppression and J_c degradation. The degradation is gradual but significant with increasing Zn content. Both YBCO phases highlight a reduction superconducting performance due to Zn doping. Such findings emphasize the critical role of maintaining CuO_2 plane integrity and avoiding high concentrations of nonmagnetic dopants in optimizing the transport and magnetic properties of high-T_c cuprate superconductors. Shortly, Zn strongly suppresses the superconducting gap by acting as a pair-breaker.

To sum up, Y-123 superconducting phase presented higher tolerance to Zn-induced disorder, preserving better superconducting and magnetic properties, whereas Y-358 phase, despite retaining higher T_c at low doping, is structurally and magnetically more fragile under excess Zn doping. The Y-358 phase, promising for high-T_c applications due to its structural complexity and higher oxygen content, remains difficult to synthesize phase-pure and stoichiometrically consistent because of intrinsic instability and intergrowth with other YBCO phases. Besides, the practical relevance of this work lies not in the direct application of highly Zn-doped YBCO ceramics, but in providing a mechanistic framework for defect engineering and performance optimization in cuprate superconductors.

Author contributions

GG, OO, SK, TS and OO conceived the idea for the project and designed the experiments. GY, OO, SK, and SS performed methodology, project administration, investigation also performed materials production. EAT, TS, GG, and OO performed experimental measurement and resources, formal analysis, review and editing. EAT, OO, SS, and GY performed writing—original draft, writing—review and editing. All authors discussed the results and commented on the manuscript.

Funding

Open access funding provided by the Scientific and Technological Research Council of Türkiye (TÜBİTAK). The authors have not disclosed any funding.

Data availability

No datasets were generated or analyzed during the current study.

Declarations

Conflict of interest The authors declare no competing interests.

Open Access This article is licensed under a Creative Commons Attribution 4.0 International License, which permits use, sharing, adaptation, distribution and reproduction in any medium or format, as long as you give appropriate credit to the original author(s) and the source, provide a link to the Creative Commons licence, and indicate if changes were made. The images or other third party material in this article are included in the article's Creative Commons licence, unless indicated otherwise in a credit line to the material. If material is not included in the article's Creative Commons licence and your intended use is not permitted by statutory regulation or exceeds the permitted use, you will need to obtain permission directly from the copyright holder. To view a copy of this licence, visit http://creativecommons.org/licenses/by/4.0/.

References

1. M. Kakihana, L. Borjesson, S. Eriksson, P. Svedlindh, Fabrication and characterization of highly pure and homogeneous $YBa_2Cu_3O_7$ superconductors from sol–gel derived powders. J. Appl. Phys. **69**(2), 867–873 (1991)
2. A. Ozturk, I. Duzgun, S. Celebi, The effect of partial Lu doping on magnetic behaviour of YBCO (123) superconductors. J. Alloy. Compd. **495**, 104–107 (2010)
3. X. Liu, J. Jia, Y. Oshima, Electron energy-loss spectroscopy study on relationship between oxygen deficiency sites

and transition temperature of YBCO. Jpn. J. Appl. Phys. **64**(9), 093001 (2025)
4. Z.W. Anderson, Y. Tang, V. Nagarajan, M.K. Chan, C.J. Dorow, G. Yu, M. Greven, Gapped commensurate antiferromagnetic response in a strongly underdoped model cuprate superconductor. npj Quantum Mater. **10**(1), 93 (2025)
5. Q. Chen, A. Moskal, Y. Wang, B.D.E. McNiven, A.A. Aczel, W. Tian, B.D. Gaulin, Competing pair density wave and uniform d-wave superconductivity in phase-separated 214 cuprates at the 1/8 anomaly. Phys. Rev. B **112**(17), 174506 (2025)
6. M.A. Rodriguez, A. Navrotsky, F. Licci, Thermochemistry of $YBa_2Cu_{3-x}M_xO_y$ (M = Ni, Zn). Phys. C: Superconduct. Appl. **329**(2), 88–94 (2000)
7. A.I. Abou Aly, N.H. Mohammed, R. Awad, H.A. Motaweh, D. El-Said Bakeer, Determination of superconducting parameters of $GdBa_2Cu_3O_{7-\delta}$ added with nanosized ferrite $CoFe_2O_4$ from excess conductivity analysis. J. Supercond. Novel Magn. **25**(7), 2281–2290 (2012)
8. M.M. Aye, S. Mejia, H. Huhtinen, P. Paturi, Influence of Rare-Earth Variations on the Superconducting Properties of YBCO Films With and Without Artificial Pinning Centers. IEEE Trans. Appl. Supercond. (2026). https://doi.org/10.1109/TASC.2026.3666832
9. M.A. Mohammed, N. Alharbi, I.I. Marhoon, F. Alshaeer, M. Al-Bahrani, G. Abdulkareem-Alsultan, M.F. Nassar, Engineering superconducting characteristics of electrospun YBCO@CNT core–shell nanofibers through BZO doping. Emergent Mater. **9**(1), 2 (2026)
10. F. Zhao, B. Zhang, X. Su, Y. Zhao, X. Zhang, Mechanism of solid solution-driven texture induced by Ag doping in YBCO superconductor. Adv. Sci. **13**(22), e22923 (2026)
11. C. Condo, S. Mejia, M.M. Aye, E. Rivasto, H. Huhtinen, P. Paturi, Balancing structure and performance: optimized BZO nanorod doping in Ca-interlayered YBCO multilayers. IEEE Trans. Appl. Supercond. (2026). https://doi.org/10.1109/TASC.2026.3656256
12. Y. Koike, T. Adachi, Impurity and magnetic field effects on the stripes in cuprates. Phys. C: Supercond. Appl. **481**, 115–124 (2012)
13. H. Hakoishi, T. Naito, Interactions between organic and inorganic additives during the degreasing of green compacts for the crystal growth of Ag-added Gd–Ba–Cu–O superconductor bulks. Ceram. Int. **51**(21), 33239–33244 (2025)
14. R.A.M. Arebat, M.M.A. Kechik, H. Baqiah, C.S. Kien, L.K. Pah, K.K.M. Shariff, M. Miryala, Impact of calcination temperature on the microstructure and superconductivity of $YBa_2Cu_3O_{7-\delta}$ ceramic prepared via modified thermal decomposition method. J. Aust. Ceram. Soc. **61**(4), 1375–1386 (2025)
15. A. Stangl, A. Kethamkuzhi, H. Roussel, C. Pop, X. Obradors, T. Puig, A. Badel, Fast track to the overdoped regime of superconducting $YBa_2Cu_3O_{7-\delta}$ thin films via electrochemical oxidation. Adv. Funct. Mater. (2025). https://doi.org/10.48550/arXiv.2512.01146
16. A. Krishnadas, Y. Fujisawa, M. Pardo-Almanza, Y. Obata, K. Yamagami, Y. Okada, Significant electron filling imbalance between chains and planes at the surface of Ca-doped $YBa_2Cu_3O_{7-x}$ films. Phys. Rev. B **111**(20), 205113 (2025)
17. C.M. Cheong, S.K. Chen, First principle calculation of lattice, electronic structures and hole concentration of Ca-doped YBCO, in *Materials Science Forum*. (Trans Tech Publications Ltd., 2025), pp.3–9
18. F.U.L.Y.A. Karaçora, İ Ergin, M. Gürsul, B. Özçelik, Sodium–lithium co-doping driven enhancement of structure, superconductivity, and vortex pinning in Bi-2212 superconductors. J. Mater. Sci. Mater. Electron. **37**(6), 424 (2026)
19. I. Bouchoucha, F.B. Azzouz, M. Annabi, M. Zouaoui, M.B. Salem, The study on the ZnO and added YBCO system: investigation of microstructure and transport properties. Phys. C: Supercond. **470**(4), 262–268 (2010)
20. E. Asikuzun, O. Ozturk, G.A. Aydemir, A.T. Tasci, The effect of zinc on the structural, electrical, and mechanical properties of YBCO-123 superconducting nanoparticles prepared by an acetate-based sol–gel process. J. Supercond. Novel Magn. **32**(11), 3415–3423 (2019)
21. J. He, Y. Wang, W. Li, Y. Zhu, X. Liu, D. Zhou, Y. Zhang, X. Yao, C. Cai, Effects of Zn doping on superconducting properties of melt textured Y–Ba–Cu–O bulk superconductors. Supercond. Sci. Technol. **35**(7), 074005 (2022)
22. P. Li, Y. Wang, Y. Tian, J. Wang, X. Niu, J. Wang, D. Wang, X. Wang, Superconductivity without dependence on valence electron density in Zn-doped YBCO systems. Chin. Phys. B **17**(9), 3484–3489 (2008)
23. R.K. Singhal, How the substitution of Zn for Cu destroys superconductivity in YBCO system. J. Alloy. Compd. **495**(1), 1–6 (2010)
24. A. Esmaeili, H. Sedghi, M.M. Golzan, M. Amniat-Talab, The Normal State Properties of $Y_3Ba_5Cu_{8-x}Zn_xO_{18-\delta}$ Superconductor in Bipolaron Model. J. Supercond. Nov. Magn. **24**, 2237–2242 (2011)
25. S. Adachi, C. Kasai, S. Tajima, K. Tanabe, S. Fujihara, T. Kimura, Lowered Tc of $YBa_2(Cu,Zn)_3O_{7-\delta}$ by homogenizing procedure and annealing treatments. Phys. C **351**(4), 323–328 (2001)

26. A. Aliabadi, Y. Akhavan Farshchi, M. Akhavan, A new Y-based HTSC with Tc above 100 K. Phys. C **469**, 2012–2014 (2009)
27. M.K. Wu, J.R. Ashburn, C.J. Torng, P.H. Hor, R.L. Meng, L. Gao, Z.J. Huang, Y.Q. Wang, C.W. Chu, Superconductivity at 93 K in a new mixed phase Y–Ba–Cu–O compound system at ambient pressure. Phys. Rev. Lett. **58**(9), 908–910 (1987)
28. A. Tavana, M. Akhavan, How Tc can go above 100 K in the YBCO family. Eur. Phys. J. B. **73**, 79–83 (2010)
29. Y. Slimani, E. Hannachi, M.K. Ben Salem, F.B. Azzouz, M. Ben Salem, Excess conductivity study in nano-$CoFe_2O_4$ added $YBa_2Cu_3O_{7-\delta}$ and $Y_3Ba_5Cu_8O_{18-x}$ superconductors. J. Supercond. Nov. Magn. **28**(10), 3001–3010 (2015)
30. N. Zarabinia, V. Daadmehr, F. Shahbaz Tehrani, M. Abbasi, Influence of Ag/Cu substitution on structural effect of new high temperature superconductor $Y_3Ba_5Cu_8O_{18}$. Procedia Mater. Sci. **11**, 242–247 (2015)
31. T. Metin, M. Tepe, The effect of Ag doping on the superconducting properties of $Y_3Ba_5Cu_{8-x}Ag_xO_{18-\delta}$ ceramics. J. Supercond. Nov. Magn. **30**(4), 1083–1087 (2017)
32. A. Ekicibil, S. Kilic Cetin, A.O. Ayas, A. Coskun, T. Firat, K. Kiymac, Exploration of the superconducting properties of $Y_3Ba_5Cu_8O_{18}$ with and without Ca doping by magnetic measurements. Solid State Sci. **13**(1), 1954–1959 (2011)
33. O. Ozturk, R.A.M. Arebat, A.R.A. Nefrow, F. Bulut, G. Guducu, E. Asikuzun, S. Celik, Investigation of structural, superconducting and mechanical properties of Co/Cu substituted YBCO-358 ceramic composites. J. Mater. Sci. Mater. Electron. **30**, 7400–7409 (2019)
34. M. Basoglu, I. Duzgun, A. Ozturk, Specification of some superconductivity parameters by adding lutetium to the YBCO (358) ceramic superconductor. J. Supercond. Nov. Magn. **34**, 1077–1084 (2021)
35. P. Udomsamuthirun, T. Kruaehong, T. Nikamjon, S. Ratreng, The new superconductors of YBaCuO materials. J. Supercond. Nov. Magn. **23**, 1377–1380 (2010)
36. S. Gholipour, V. Daadmehr, A.T. Rezakhani, H. Khosroabadi, F. Shahbaz Tehrani, R. Hosseini Akbarnejad, Structural phase of Y358 superconductor comparison with Y123. J. Supercond. Nov. Magn. **25**, 2253–2258 (2012)
37. M. Barakat, A. Abou-Aly, A. Awad, N. Aly, S. Ibrahim, Mechanical properties of $Y_{3-x}Nd_xBa_{5-x}Ca_xCu_8O_{18-\delta}$ samples. J. Alloy. Compd. **652**, 158–164 (2015)
38. I. Duzgun, The investigation of the lattice strains and crystallite sizes of Y358 and Y123 high-temperature superconductors. Turk. J. Phys. **42**, 378–385 (2018)
39. Y. Slimani, E. Hannachi, F. Ben Azzouz, M. Ben Salem, Impact of planetary ball milling parameters on the microstructure and pinning properties of polycrystalline superconductor $Y_3Ba_5Cu_8O_y$. Cryogenics **92**, 5–11 (2018)
40. U. Topal, M. Akdogan, H. Ozkan, Electrical and structural properties of $RE_3Ba_5Cu_8O18$ (RE = Y, Sm, and Nd) superconductors. J. Supercond. Nov. Magn. **24**, 2099–2102 (2011)
41. A.O. Ayas, A. Ekicibil, S.K. Cetin, A. Coskun, A.O. Er, Y. Ufuktepe, T. Firat, K. Kıymac, The structural, superconducting and transport properties of the compounds $Y_3Ba_5Cu_8O_{18}$ and $Y_3Ba_5Ca_2Cu_8O_{18}$. J. Supercond. Nov. Magn. **24**, 2179–2183 (2011)
42. S. Sujinnapram, P. Udomsamuthirun, T. Nilkamjon, S. Ratreng, XRD spectra of new YBaCuO superconductors. Bull. Mater. Sci. **34**, 1053–1057 (2011)
43. G. Guducu, O. Ozturk, S. Kurnaz, E.A. Tokeser, S. Safran, G. Yildirim, Assessment of superconducting and structural stability of advanced Y-123 and Y-358 ceramics with Tb/Y substitution in main matrices. J. Alloy. Compd. **997**, 174838 (2024)
44. O. Ozturk, G. Guducu, S. Kurnaz, T. Seydioğlu, S. Safran, Structural and mechanical dynamics of Y-358 superconductors influenced by Tb/Y and Zn/Cu substitutions. J. Supercond. Nov. Magn. **38**, 38 (2025)
45. M.K. Ben Salem, A. Hamrita, E. Hannachi, Y. Slimani, M. Ben Salem, F. Ben Azzouz, The study on SiO_2 nanoparticles and nanowires added YBCuO: microstructure and normal state electrical properties. Physica C Superconduct. **498**, 38–44 (2014)
46. A. Hamrita, F. Ben Azzouz, A. Madani, M. Ben Salem, Magnetoresistivity and microstructure of $YBa_2Cu_3O_y$ prepared using planetary ball milling. Physica C Superconduct. **472**, 34–38 (2012)
47. Y. Zhao, C.H. Cheng, J.S. Wang, Flux pinning by NiO-induced nano-pinning centres in melt-textured YBCO superconductor. Supercond. Sci. Technol. **18**(2), S43–S46 (2004)
48. M. Akyol, A.O. Ayas, G. Akca, S.K. Cetin, A. Ekicibil, Effect of Ca doping on thermally activated flux flow in the $Y_3Ba_5Cu_8O_{18}$ superconductor. Bull. Mater. Sci. **38**, 1231–1237 (2015)
49. A. El-Aziz, M. Ahmed, H.A. Afifi, I.Z. Hager, N.S. Abdel Aal, S.H. Naqib, Unusual enhancement of normal and superconducting state properties of $(100–x)YBa_2Cu_3O_{7-\delta}$ + xNi (x = 1, 2.5, 5, 7.5, 10, and 15 wt%) composites with low level of Ni additives. J. Supercond. Nov. Magn. **33**, 661–674 (2019)
50. Y. Slimani, E. Hannachi, A. Hamrita, M.K. Ben Salem, F. Ben Azzouz, A. Manikandan, M. Ben Salem, Comparative investigation of the ball milling role against hand grinding on microstructure, transport and pinning properties of

$Y_3Ba_5Cu_8O_{18\pm\delta}$ and $YBa_2Cu_3O_{7-\delta}$. Ceram. Int. **44**, 19950–19957 (2018)
51. B. Cakır, A. Aydiner, K. Karaoglu, S. Duman, E. Yanmaz, Flux pinning in YBCO single crystal grown on Y_2O_3 layer. J. Supercond. Novel Magn. **27**, 1123–1129 (2014)
52. K. Yakinci, O. Cicek, Role of multi-walled carbon nanotube addition in superconducting properties of $Bi_2Sr_2CaCu_2O_{8+s}$ glass-ceramic superconductors. Acta Phys. Pol. A **143**(4), 298–298 (2023)
53. S. Abdelhaleem, M. Noun, N.M. Yousif, M.S. Shalaby, Impact of carbon nanotubes on superconducting properties and ferromagnetism of indium-doped Bi-2212 superconductors: critical current density enhancement. Phys. B: Condens. Matter **697**, 416704 (2025)
54. J.L. Tallon, C. Bernhard, H. Shaked, R.L. Hitterman, J.D. Jorgensen, Generic superconducting phase behavior in high-T_c cuprates: T_c variation with hole concentration in $YBa_2Cu_3O_{7-\delta}$. Phys. Rev. B **51**, 12911–12914 (1995)
55. D.M. Newns, P.C. Pattnaik, C.C. Tsuei, Role of Van Hove singularity in high-temperature superconductors: mean field. Phys. Rev. B **43**(4), 3075 (1991)
56. R. Terzioglu, Evaluation of magnetotransport properties of Au added YBCO ceramics: combination of experimental and advanced theoretical approaches. J. Mater. Sci. Mater. Electron. **32**(4), 4737–4748 (2021)
57. A. Mohanta, *Superconducting order parameter fluctuation in doped and composite cuprate superconductors* (National Institute of Technology, Rourkela, 2011)
58. T. Sato, H. Nakane, S. Yamazaki, N. Mori, S. Hirano, S. Yoshizawa, T. Yamaguchi, Analysis of fluctuation conductivity in melt-textured $DyBa_2Cu_3O_y$ superconductors. Physica C (2003). https://doi.org/10.1016/s0921-4534(03)00992-4
59. S. Duman, B. Cakır, A. Aydiner, Fluctuation-induced conductivity analysis of Y_2O_3-layered YBCO single crystal. J. Supercond. Nov. Magn. **29**(9), 2275–2280 (2016)
60. S.M. Hasnain, M. Mumtaz, N.A. Khan, Optimum synthesis temperature of $(Cu_{1-x}Tl_x)Ba_2Ca_3Cu_4O_{12-\delta}$ superconductor. J. Supercond. Nov. Magn. **24**(5), 1653–1657 (2011)
61. C.P. Bean, Magnetization of high-field superconductors. Rev. Mod. Phys. **36**, 31–39 (1964)
62. T. Higuchi, S.I. Yoo, M. Murakami, Comparative study of critical current densities and flux pinning among a flux-grown $NdBa_2Cu_3Oy$ single crystal, melt-textured Nd–Ba–Cu–O, and Y–Ba–Cu–O bulks. Phys. Rev. B **59**, 1514 (1999)
63. A.A. Arais, M.S. Shams, E. Elbehiry, The effect of Ni–Zn ferrite doping on the superconductivity of $Y_3Ba_5Cu_8O_{18}$ nanocomposite materials. AIP Adv. **10**, 115012 (2020)
64. M.A. Almessiere, Y. Slimani, E. Hannachi, R. Algarni, F.B. Azzouz, Impact of Dy_2O_3 nanoparticles additions on the properties of porous YBCO ceramics. J. Mater. Sci. Mater. Electron. **30**(21), 19747–19756 (2019)
65. H. Hiraka, Y. Hayashi, S. Wakimoto, M. Takeda, K. Kakurai, T. Adachi, K. Yamada, Incommensurate spin correlations induced by magnetic Fe ions substituted into overdoped $Bi_{1.75}Pb_{0.35}Sr_{1.90}CuO_{6+z}$. Phys. Rev. B: Condens. Matter Mater. Phys. **81**(14), 144501 (2010)
66. M.N. Ozalp, A.T. Ulgen, U. Erdem, G. Yildirim, C. Terzioglu, Optimized superconducting performance and vortex dynamics in silver nanopowder-substituted Bi-2212 ceramics: flux pinning, magnetoresistivity, and energy dissipation analyses. Magnetoresist. Energy Dissip. Analy. (2025). https://doi.org/10.2139/ssrn.5915430

Publisher's Note Springer Nature remains neutral with regard to jurisdictional claims in published maps and institutional affiliations.